Cell Reports

Article

The functional and anatomical characterization of three spinal output pathways of the anterolateral tract

Graphical abstract

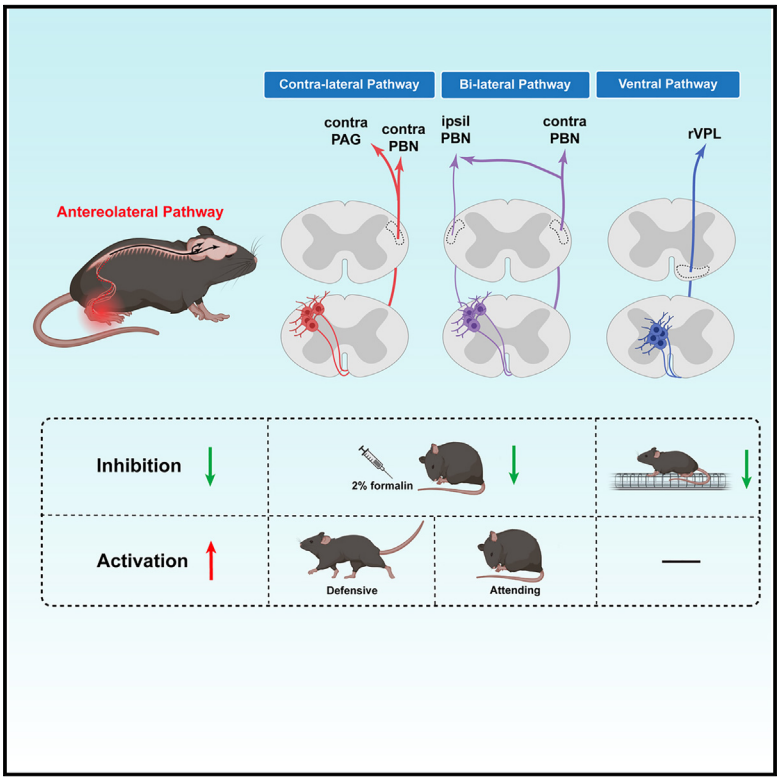

Highlights

- The anterolateral pathway includes two tracts: a lateral and a ventral pathway
- The lateral pathway consists of two subpathways: a bilateral and a contralateral pathway
- The three anterolateral pathways mediate distinct nociceptive and sensorimotor behaviors

Authors

Haichao Chen, Isabel H. Bleimeister, Eileen K. Nguyen, ..., Kelly M. Smith, Mark L. Baccei, Sarah E. Ross

Correspondence

saross@pitt.edu

In brief

Chen et al. identify three subclasses within the anterolateral pathway that have different anatomical and physiological properties and mediate distinct nociceptive and sensorimotor behaviors.

Chen et al., 2024, Cell Reports *43*, 113829
March 26, 2024
https://doi.org/10.1016/j.celrep.2024.113829

CellPress

Cell Reports

CellPress
OPEN ACCESS

Article

The functional and anatomical characterization of three spinal output pathways of the anterolateral tract

Haichao Chen,[1,2] Isabel H. Bleimeister,[2,3] Eileen K. Nguyen,[2,3] Jie Li,[5] Abby Yilin Cui,[2] Harrison J. Stratton,[2,4] Kelly M. Smith,[2,4] Mark L. Baccei,[5] and Sarah E. Ross[2,4,6,7,*]

[1]Tsinghua Medicine, Tsinghua University, Beijing 100084, China
[2]Pittsburgh Center for Pain Research, University of Pittsburgh, Pittsburgh, PA 15213, USA
[3]Medical Scientist Training Program, University of Pittsburgh, Pittsburgh, PA 15213, USA
[4]Department of Neurobiology, University of Pittsburgh, Pittsburgh, PA 15213, USA
[5]Department of Anesthesiology, Pain Research Center, University of Cincinnati Medical Center, Cincinnati, OH 45267, USA
[6]Department of Anesthesiology, University of Pittsburgh, Pittsburgh, PA 15213, USA
[7]Lead contact
*Correspondence: saross@pitt.edu
https://doi.org/10.1016/j.celrep.2024.113829

SUMMARY

The nature of spinal output pathways that convey nociceptive information to the brain has been the subject of controversy. Here, we provide anatomical, molecular, and functional characterizations of two distinct anterolateral pathways: one, ascending in the lateral spinal cord, triggers nociceptive behaviors, and the other one, ascending in the ventral spinal cord, when inhibited, leads to sensorimotor deficits. Moreover, the lateral pathway consists of at least two subtypes. The first is a contralateral pathway that extends to the periaqueductal gray (PAG) and thalamus; the second is a bilateral pathway that projects to the bilateral parabrachial nucleus (PBN). Finally, we present evidence showing that activation of the contralateral pathway is sufficient for defensive behaviors such as running and freezing, whereas the bilateral pathway is sufficient for attending behaviors such as licking and guarding. This work offers insight into the complex organizational logic of the anterolateral system in the mouse.

INTRODUCTION

A fundamental understanding of how noxious input is conveyed to the brain for the conscious perception of pain originated from the observation that patients with anterolateral spinal cord lesions had a selective loss of pain and temperature on the contralateral side.[1–3] *In vivo* recordings in monkeys suggested a model where the sensory discriminative component of pain is conveyed to the forebrain via a pathway involving spinothalamic (or trigeminothalamic) neurons from lamina V that target the ventrobasal complex (ventral posterior lateral (VPL) or ventral posterior medial (VPM) nuclei).[1] Nociceptive information was known to be conveyed in parallel by lamina I spinal output neurons, which were thought to contribute predominantly to the affective component of pain through multisynaptic pathways that provide input to the limbic system.[4,5] According to this scheme, separate pathways convey sensory discriminative and sensory affective components of pain, respectively, which are represented in distinct regions of the cortex.

An alternate proposal of the neural pathways contributing to the pain percept was presented by Craig,[6,7] who conceptualized nociception as a component of interoception rather than somatosensation. In his model, nociceptive information underlying the pain percept is primarily conveyed to the brain by spinal output neurons in lamina I rather than those in lamina V.[6,7] Craig[6,7] argued that, in addition to their collaterals at a number of brain regions involved in homeostasis, the dominant projection of lamina I spinal output neurons is a region of the thalamus that is connected to the insula and that the insula is the key cortical locus for conscious pain perception.[8–11]

In the mouse, several groups have investigated the anatomy and functional roles of spinoparabrachial (SPB) neurons for pain behaviors. Many lamina I spinal output neurons can be backlabeled from the contralateral parabrachial nucleus (PBN) or the caudal ventral lateral medulla (CVLM), whereas only subsets of these neurons extend collaterals to other brain regions, such as the periaqueductal gray (PAG).[12–14] These neurons have been variously classified based on a number of criteria, including neurochemical properties, somatic morphology, and their functional response properties to natural stimuli, revealing a high degree of heterogeneity.[15–19] More recently, it was found that the developmental factor Phox2a selectively labels the SPB neurons.[20,21] Finally, by using Cre alleles that target distinct subpopulations of SPB neurons, it was found that activation of PBN terminals of Tac1 or Tacr1 spinal neurons (which show partially overlapping expression profiles) gives rise to exacerbated responses to

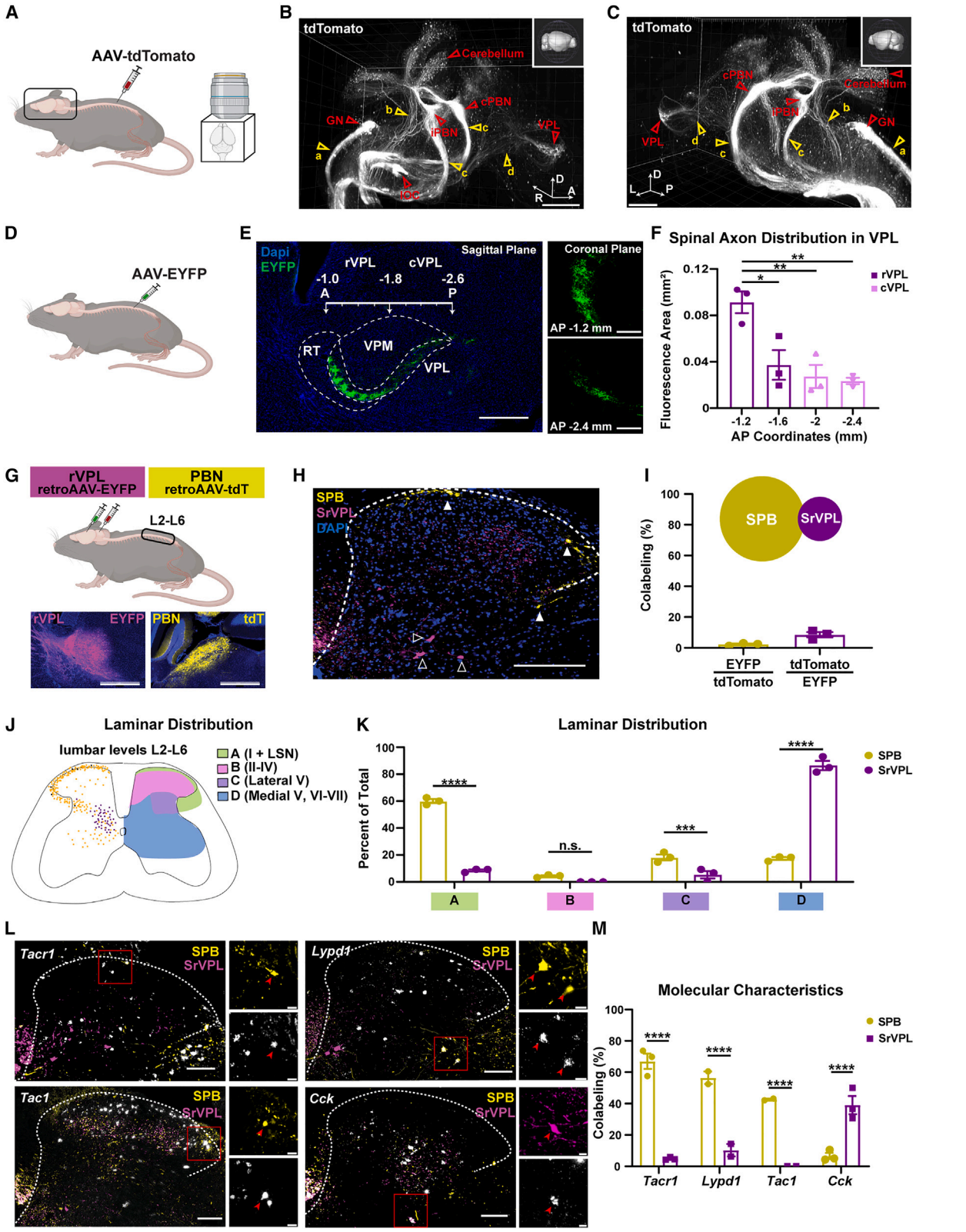

(legend on next page)

noxious input and strong aversion, whereas activation of Gpr83 neurons, at least at low intensity, can be appetitive.[22,23] Thus, activation of SPB neurons can give rise to a complex array of behaviors, depending on the cells involved and the site of stimulation.

Here, we revisited the question of which spinal output neurons are involved in nociception by exploring the anatomy and function of three major spinal output pathways that ascend within the anterolateral system, both spinothalamic and SPB ,providing a detailed picture of the complex organization of this system.

RESULTS

Although spinal projection neurons that respond to noxious input are found in many different laminae of the spinal cord, the specific roles of different output neurons in nociception remain unclear.[24] To address this issue, we injected an AAV encoding tdTomato (tdT) into the right spinal cord at the lumbar enlargement and used light sheet imaging to visualize the projections of spinal output neurons in the brain (Figure 1A). We could readily identify several major ascending axon tracts, as illustrated in images of the whole brain from two different orientations (Figures 1B and 1C). These included the postsynaptic dorsal column pathway (a), which targeted the ipsilateral gracile nucleus (GN); the spinocerebellar pathway (b), which showed predominantly ipsilateral projections terminating in both the anterior and posterior lobes of the cerebellum; the SPB pathway (c), which was bilateral and targeted the PBN on both sides; and a spinothalamic pathway (d), which was exclusively contralateral and showed prominent projections in the VPL nucleus (see also Video S1).

This pattern of ascending fibers raised the possibility that retrograde labeling from VPL and the PBN might distinguish two major spinal output pathways that have been implicated in nociception.[25,26] To explore the feasibility of this approach, we began by characterizing the anatomy of the axonal projections to the VPL in more detail (Figure 1D). We observed that the innervation of the VPL from lumbar spinal output neurons was non-uniform, with the rostral VPL (rVPL) received a significantly higher density of innervation than the caudal VPL (cVPL) (Figures 1E and 1F). Given this biased distribution of innervation, we targeted the rVPL to label spino-rVPL (SrVPL) neurons. The PBN was targeted in parallel to label SPB neurons, using distinct viruses (Figures 1G and 1H) or tracers (Figures S1A–S1C). We found that SPB neurons and SrVPL neurons in the lumbar spinal cord are almost entirely non-overlapping populations, with SPB neurons outnumbering SrVPL neurons three to one (Figures 1I and S1D), consistent with previous studies.[19,27] The majority (60% ± 3%) of SPB neurons were found in lamina I and the lateral spinal nucleus, with some neurons observed in the lateral aspect of lamina V (Figures 1J and 1K), as described previously.[19,21,28] In contrast, the majority (86% ± 6%) of SrVPL neurons were located in the medial aspect of laminae V–VII, consistent with previous reports.[29–32]

Next, we investigated the molecular characteristics of these spinal output neurons. Virtually all SPB and SrVPL neurons co-expressed *Slc17a6* (*Vglut2*) (Figures S1E and S1F), indicating that they are excitatory. Many SPB neurons were found to express *Tacr1*, *Lypd1*, and *Tac1*, as reported previously,[23,33] whereas few SrVPL neurons were labeled with these markers. In contrast, significantly more SrVPL neurons than SPB neurons expressed *Cck* (Figures 1L, 1M, and S1G). Thus, at least at lumbar levels in mice, retrograde labeling from the rVPL and PBN captures largely separate populations of spinal output neurons that show distinct laminar distributions and molecular characteristics.

To visualize the complete anatomy of SPB and SrVPL neurons, we selectively labeled each population emerging from the right lumbar enlargement with different fluorophores (Figures 2A, 2B, and S2A). As expected, virally labeled somata were found

Figure 1. SPB neurons and SrVPL neurons are distinct populations

(A) Strategy to visualize axons of spinal output neurons using light sheet fluorescence microscopy.

(B and C) Representative images of axons from spinal output neurons. Scale bars: 700 μm (B) and 1 mm (C). Inset: the orientation of the brain (R, right; L, left; A, anterior; P, posterior; D, dorsal). Red arrowheads indicate targets; yellow arrowheads indicate axons tracts. a, dorsal column pathway; b, spinocerebellar tract; c, spinoreticular tract; d, spinothalamic tract.

(D) Strategy to label spinal output neurons that innervate the VPL.

(E) Representative images of brain sections showing the axonal distribution of spinothalamic neurons in the VPL in a sagittal plane (left) and coronal planes (right). Scale bars: 500 μm (sagittal section) and 200 μm (coronal sections). The AP location is indicated.

(F) Quantification of the fluorescence area in the VPL across AP coordinates. Data are mean ± SEM, with symbols indicating individual mice (n = 3 mice). One-way ANOVA, $^{**}p < 0.01$, $^{*}p < 0.05$.

(G) Strategy for retrograde labeling of SPB and SrVPL neurons. Shown are representative images of EYFP and tdT expression in rVPL and PBN, respectively. Scale bar: 1 mm.

(H) Representative image of SPB and SrVPL neurons in the lumbar spinal cord. Solid arrowheads indicate SPB neurons in the superficial dorsal horn and lateral lamina V. Outlined arrowheads indicate SrVPL in laminae V–VII. Scale bar: 200 μm.

(I) Quantification of colabeling between SPB and SrVPL neurons in L2–L6. Data are mean ± SEM, with symbols indicating individual mice (n = 3 mice with 15–20 sections per mouse).

(J) Laminar distribution of SPB and SrVPL neurons in the lumbar spinal cord of a representative mouse. Orange dots represent SPB neurons; purple dots represent SrVPL neurons. Data are from 36 18-μm hemisections spanning L2–L6.

(K) Quantification of the laminar distribution of SPB and SrVPL neurons in L2–L6. Data are mean ± SEM, with symbols representing individual mice (n = 3 mice with 15–20 sections per mouse). two-way ANOVA with Sidak correction, $^{***}p < 0.001$, $^{****}p < 0.0001$.

(L) Representative images of immuno-fluorescence *in situ* hybridization (FISH) using probes against *Tacr1*, *Lypd1*, *Tac1*, or *CCK*, as indicated, and antibodies against tdT in retrogradely labeled SPB neurons and EYPF in retrogradely labeled SrVPL neurons. Arrows indicate SPB or SrVPL neurons that are colabeled with the indicated FISH probes. Scale bar: 100 μm.

(M) Quantification of the proportion of SPB or SrVPL neurons that express the indicated molecular marker. Data are mean ± SEM, with symbols indicating individual mice (n = 2–3 mice with 9–15 sections per mouse). two-way ANOVA with Sidak correction, $^{****}p < 0.0001$.

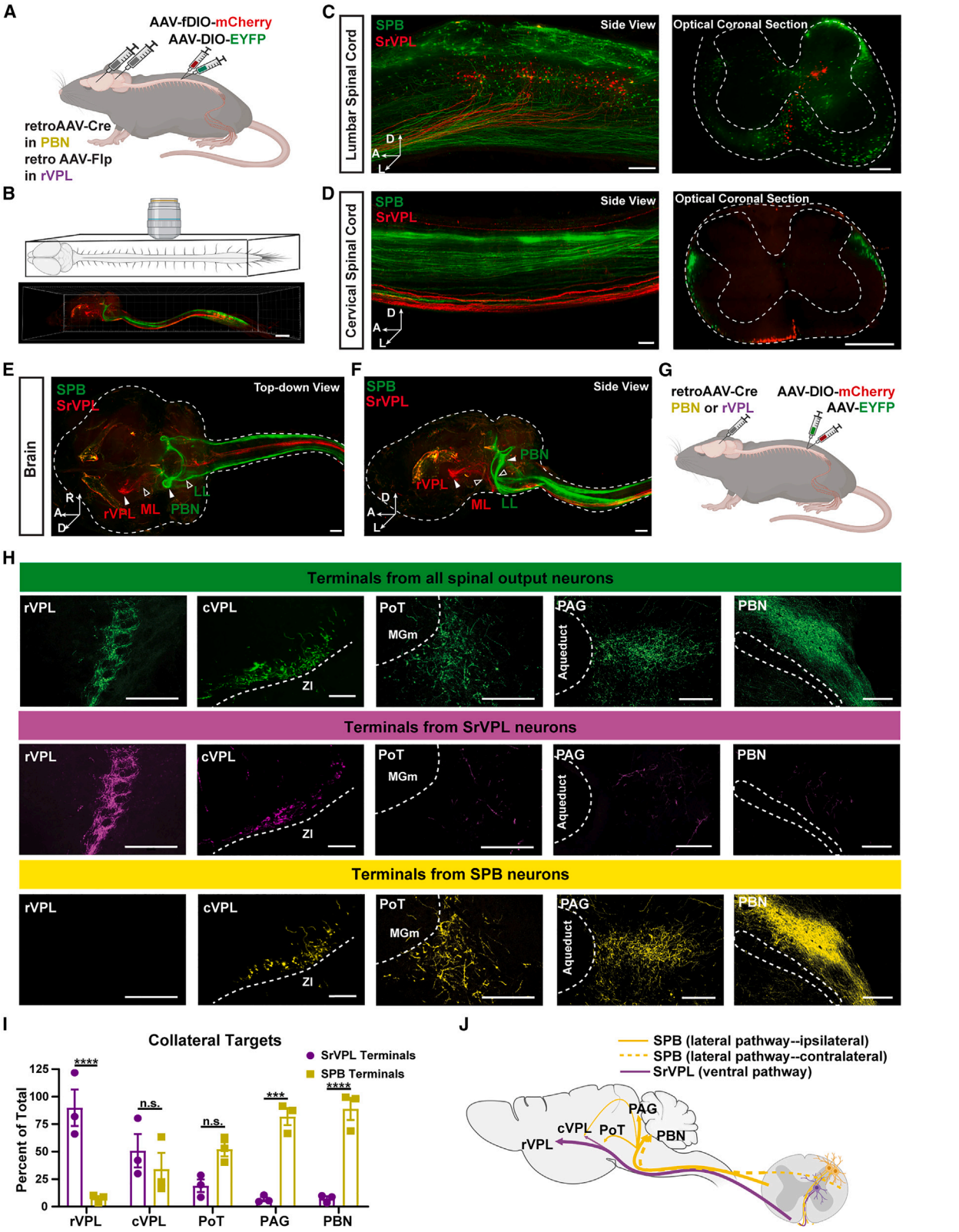

(legend on next page)

in the right lumbar cord, with SPB neurons located primarily in the superficial dorsal horn and SrVPL neurons located primarily in the deep dorsal horn (Figure 2C). At the cervical level, the red and green axon tracts from lumbar spinal projection neurons were clearly distinct; SrVPL neurons ascended contralaterally in the ventral white matter, whereas SPB neurons ascended bilaterally in the lateral white matter (Figure 2D). The SrVPL and SPB neurons also differed with respect to their ascending trajectories within the brain, as evidenced by the fact that axons from SrVPL neurons ascended contralaterally along the medial lemniscus, whereas axons from SPB neurons ascended bilaterally through the lateral lemniscus (Figures 2E, 2F, S2B, and S2C; Video S2).

Spinal projection neurons are known to extend collateral axons to multiple brain targets.[13,34] For an in-depth picture of target innervation by these two pathways, we used a dual labeling approach where a specific population was labeled with mCherry (SPB or SrVPL neurons), while all spinal output neurons were labeled with EYFP (Figure 2G). We found that SPB neurons sent very few axonal projections to the rVPL (7.6% ± 2% of the total) and that SrVPL neurons extended few axonal projections to the PBN (7.4% ± 2% of the total), confirming our previous observation that SPB neurons and SrVPL neurons are largely non-overlapping populations (Figure 2H). Within the thalamus, SPB neurons sent numerous collateral axons to the posterior triangle (PoT) and medial thalamus, whereas the density from SrVPL axons to these structures was minor. Notably, both SPB neurons and SrVPL neurons targeted the cVPL, consistent with the notion that the rVPL and cVPL are distinct in terms of the types of sensory input they receive, as suggested previously.[35] SPB axons also innervated several other brain nuclei, including the lateral PAG, the superior colliculus, and the lateral reticular formation (LRF), all of which received relatively minor input from SrVPL neurons (Figures 2H, 2I, and S2D). Thus, SPB and SrVPL neurons are distinct with respect to their ascending pathways and their targets within the brain (Figure 2J). Together, these findings support the idea that the anterolateral system in mice comprises at least two distinct pathways with axons that ascend in different regions of the spinal cord: an anterior pathway made up of SrVPL neurons (also called the ventral spinothalamic pathway), as described previously for cats and macaques,[36–38] and a lateral pathway made up of SPB neurons that extend collaterals to the PAG and several regions of the thalamus, as described previously for several species, including the mouse.[21,39–41]

To examine the functions of these two spinal output populations, we performed gain-of-function experiments. Pathway selectivity was achieved through the injection of a retrograde AAV encoding Cre into the target of interest (PBN or rVPL) and a Cre-dependent AAV encoding either hM3D-mCherry or mCherry alone into the right spinal cord at the lumbar enlargement (Figure 3A). Treatment with clozipine-n-oxide (CNO) induced robust Fos expression in over 80% of hM3D-expressing neurons and in less than 10% of mCherry-expressing neurons, consistent with robust and specific activation (Figures 3B, 3C, S3A, and S3B). Upon activation of SPB neurons (i.e., the lateral pathway) from the lumbar spinal cord, mice showed spontaneous nociceptive behaviors that were suggestive of pain, including flinching, guarding, and licking of the hindpaw. In contrast, activation of lumbar SrVPL neurons (i.e., the ventral pathway) did not evoke any visible behaviors, nociceptive or otherwise (Figure 3D; Video S3). Activation of SPB neurons also resulted in freezing together with reduced ambulation, whereas the activation of SrVPL neurons had no measurable effect in hM3D-expressing mice, which were visually indistinguishable from mCherry-expressing controls (Figures S3C–S3E).

The finding that activation of the ventral pathway, which is a major spinal ascending pathway to the thalamus, did not elicit any behavioral responses defied our initial expectations. We therefore attempted optogenetic approaches to activate rVPL input with superior temporal resolution. An AAV encoding ChR2 was injected unilaterally into the lumbar cord, and optogenetic stimulation was performed in the rVPL of freely moving mice (Figure S3F). Again, we did not observe any spontaneous behavior upon stimulation of the SrVPL input to the thalamus, including nociceptive behaviors such as flinching, guarding, or licking (Figures S3G and S3H). Thus, only activation of the lateral pathway showed a clear role in nociceptive behaviors.

Over the course of these experiments, we noted that activation of SPB neurons on the right side of the lumbar level triggered behavior that was directed to the ipsilateral (right) foot. To extend this observation, we compared this behavior with that observed

Figure 2. SPB Neurons and SrVPL neurons have distinct ascending tracts and collateral targets

(A) Strategy to selectively label SPB or SrVPL neurons.

(B) Cartoon (top) and representative image (bottom) of a cleared nervous system showing fluorescently labeled SPB and SrVPL neurons, visualized using light sheet microscopy. Scale bar: 3 mm.

(C) Representative images of the lumbar spinal cord, observed from the side view, showing labeled SPB and SrVPL neurons (left) and corresponding optical coronal section (right). Arrows indicate the direction of view. Scale bars: 400 μm (side view) and 1 mm (optical coronal section).

(D) Representative images of the cervical spinal cord, observed from the side view, showing axons of labeled SPB (green) and SrVPL (red) neurons (left) and corresponding optical coronal section (right). Arrows indicate the direction of view. Scale bars: 400 μm (side view) and 1 mm (optical section). Data are representative of 3 mice.

(E and F) Representative top-down view (E) and side view (F) of axons from SPB neurons (green) and SrVPL neurons (red) in a cleared brain. Arrows indicate the direction of view. Solid arrowheads indicate VPL (red) or PBN (green); outlined arrowheads indicate the medial lemniscus (ML, red) and lateral lemniscus (LL, green). Scale bars: 1 mm.

(G) Strategy to selectively label SPB neurons (or SrVPL neurons) with mCherry and label all spinal output neurons with EYFP.

(H) Representative image showing the innervation of the indicated brain region by all spinal output neurons (top, green), SrVPL neurons (center, purple), or SPB neurons (bottom, yellow). Scale bars: 200 μm (rVPL), 100 μm (cVPL), 200 μm (PoT), 200 μm (PAG), and 200 μm (PBN).

(I) Quantification of fluorescence from SrVPL terminals or SPB terminals relative to total for a given brain structure. Data are mean ± SEM, and each dot represents an individual animal (n = 3 mice per condition). two-way ANOVA with Sidak correction, ***$p < 0.001$, ****$p < 0.0001$.

(J) Cartoon summarizing the ascending pathways and collateralization targets of SrVPL and SPB neurons.

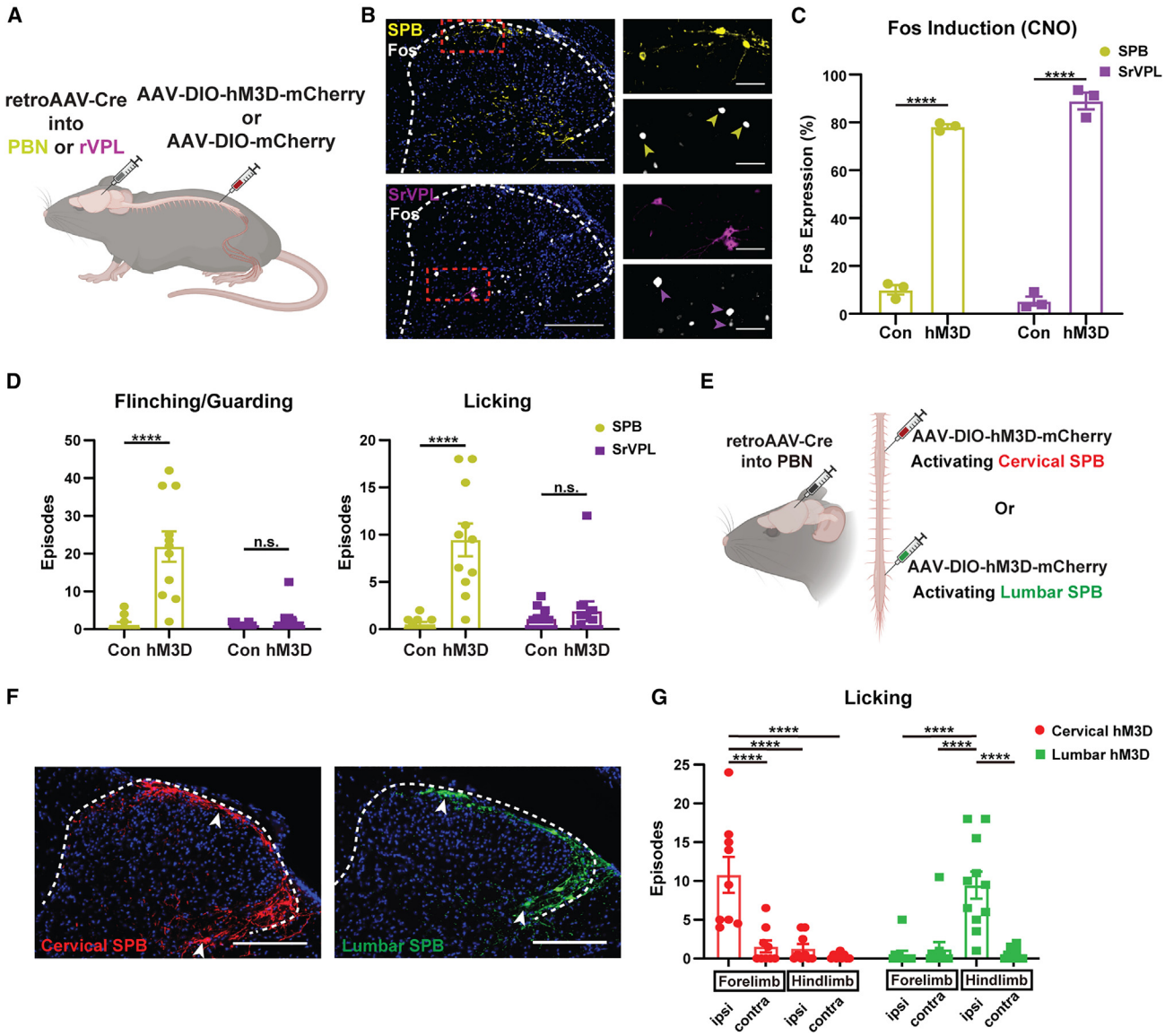

Figure 3. Activation of SPB neurons, but not SrVPL neurons, elicits nociceptive behaviors

(A) Strategy to selectively target SPB neurons or SrVPL neurons for chemogenetic activation with hM3Dq-DREADD.

(B and C) Representative images (B) and quantification (C) of Fos expression in SPB neurons or SrVPL neurons following treatment of mice with CNO. A magnified inset is shown on the right. Scale bars: 250 μm and 50 μm (inset). Yellow arrows and purple arrows point to Fos-positive SPB neurons and SrVPL neurons, respectively. Data are mean ± SEM, with symbols representing individual mice (n = 3 mice with 9–15 sections per mouse). two-way ANOVA with Sidak correction, ****$p < 0.0001$.

(D) Activation of lumbar SPB neurons induced hindpaw-oriented flinching/guarding and licking behavior, while activation of SrVPL neurons did not. Data are mean ± SEM, with symbols representing individual mice (n = 9–11 mice per group). two-way ANOVA with Sidak correction, ****$p < 0.0001$.

(E) Strategy to chemogenetically activate right cervical or right lumbar SPB neurons.

(F) Representative images of labeled cervical SPB neurons and lumbar SPB neurons. Arrowheads point to SPB neurons. Scale bar: 200 μm.

(G) Chemogenetic activation of right cervical SPB neurons induced licking of the right forelimb, whereas activation of right lumbar SPB neurons induced licking of the right hindlimb. Data are mean ± SEM, with symbols indicating individual mice (n = 9–11 mice per group). Two-way ANOVA with Sidak correction, ****$p < 0.0001$.

upon activation of right cervical SPB neurons (Figures 3E and 3F). Indeed, just as activation of right lumbar SPB neurons caused licking of the right hindlimb, activation of right cervical SPB neurons caused licking of the right forelimb (Figures 3G; Video S3). Some spinothalamic targets, such as the VPL and the posterior nucleus (Po), receive somatotopically organized inputs, which are readily visible (Figures S4A–S4D). However, the degree to which the sensory input from the lateral pathway might show somatic topography remained unclear. To visualize the underlying anatomy that might enable site-directed behaviors

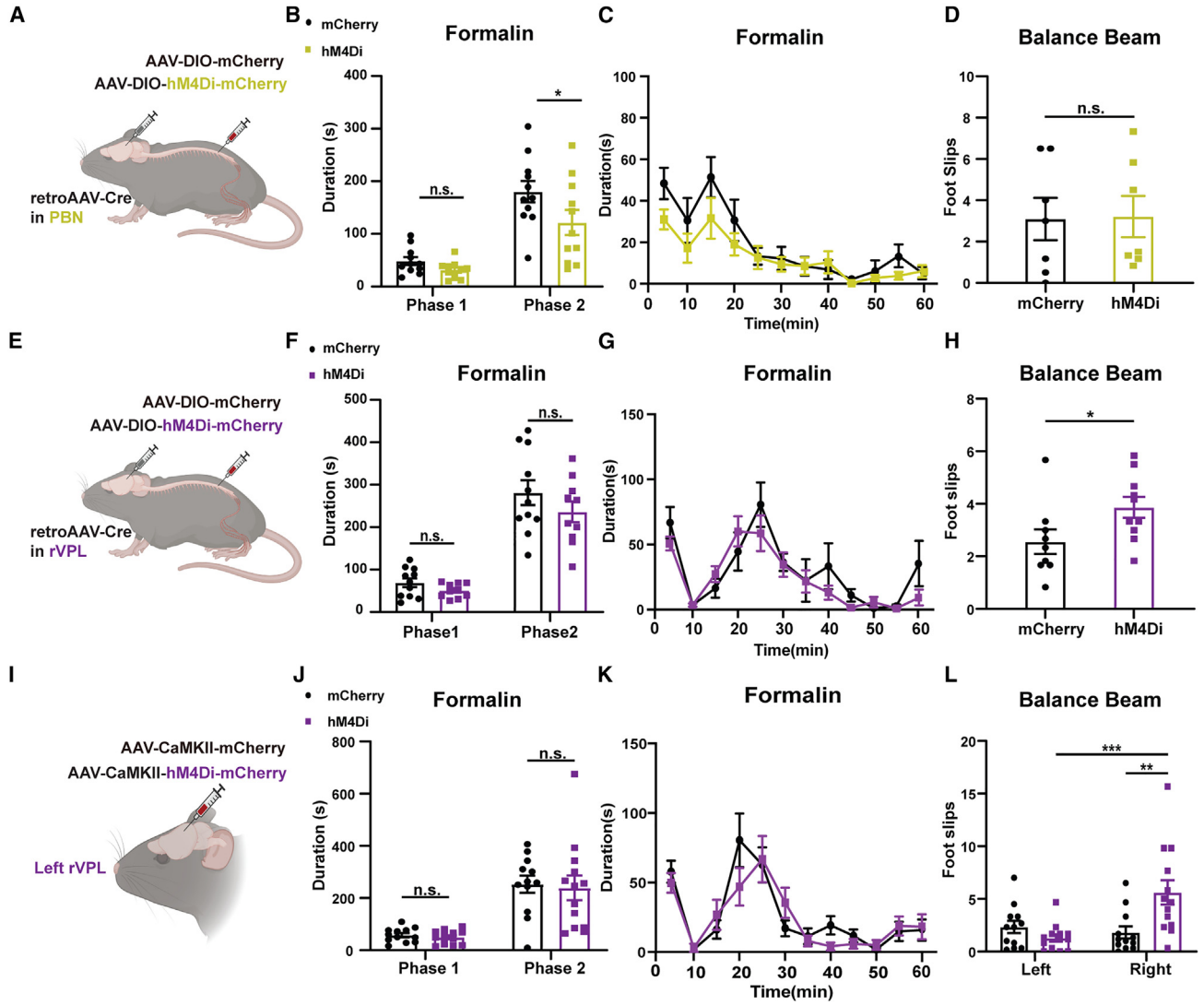

Figure 4. Inhibition of SPB neurons reduced pain behavior, whereas inhibition of SrVPL neurons or rVPL neurons reduced sensorimotor coordination

(A) Strategy to selectively target SPB neurons for chemogenetic inhibition with hM4Di-DREADD.

(B–D) Inhibition of SPB neurons resulted in a deficit in pain behavior in response to intraplantar formalin (B and C) but not sensorimotor behavior, as measured by foot slips on a narrow balance beam (D). Data are mean ± SEM, with symbols indicating individual mice (n = 7–13 mice per group). Formalin test: two-way ANOVA with Sidak correction (B), *$p < 0.05$. Balance beam: two-tailed unpaired t test; n.s. (not significant), $p > 0.05$.

(E) Strategy to selectively target SrVPL neurons for chemogenetic inhibition with hM4Di-DREADD.

(F–H) Inhibition of SrVPL neurons had no effect in the formalin test (F and G) but caused increased foot slips on a balance beam (H). Data are mean ± SEM, with symbols indicating individual mice (n = 9–11 mice per group). Formalin test: two-way ANOVA with Sidak correction (F); n.s., $p > 0.05$. Balance beam: two-tailed unpaired t test, *$p < 0.05$.

(I) Strategy to target excitatory neurons in the left rVPL for chemogenetic inhibition with hM4Di-DREADD.

(J–L) Inhibition of the left rVPL had no effect on the formalin response (J and K) but caused increased foot slips that were specific to the contralateral side (L). Data are mean ± SEM, with symbols indicating individual mice (n = 12–13 mice per group). Formalin test: two-way ANOVA with Sidak correction (J); n.s., $p > 0.05$. Balance beam: two-way ANOVA with Sidak correction, **$p < 0.01$, ***$p < 0.001$.

from activation of the lateral pathway, we compared the axonal projections of mCherry-labeled, cervical SPB neurons and EYFP-labeled, lumbar SPB neurons. Distinguishable fields of axon terminals from lumbar and cervical neurons were evident in the cVPL and the PAG, though not in the PoT or the PBN (Figures S4E–S4J). Together, these observations suggest that SPB neurons are able to guide site-oriented nociceptive behaviors and identify some brain loci where the inputs from the lateral pathway show somatic topography.

Next, we investigated the roles of spinal output neurons using inhibitory designer receptors exclusively activated by designer drugs (DREADDs) (Figure 4A). Previous work from us and others

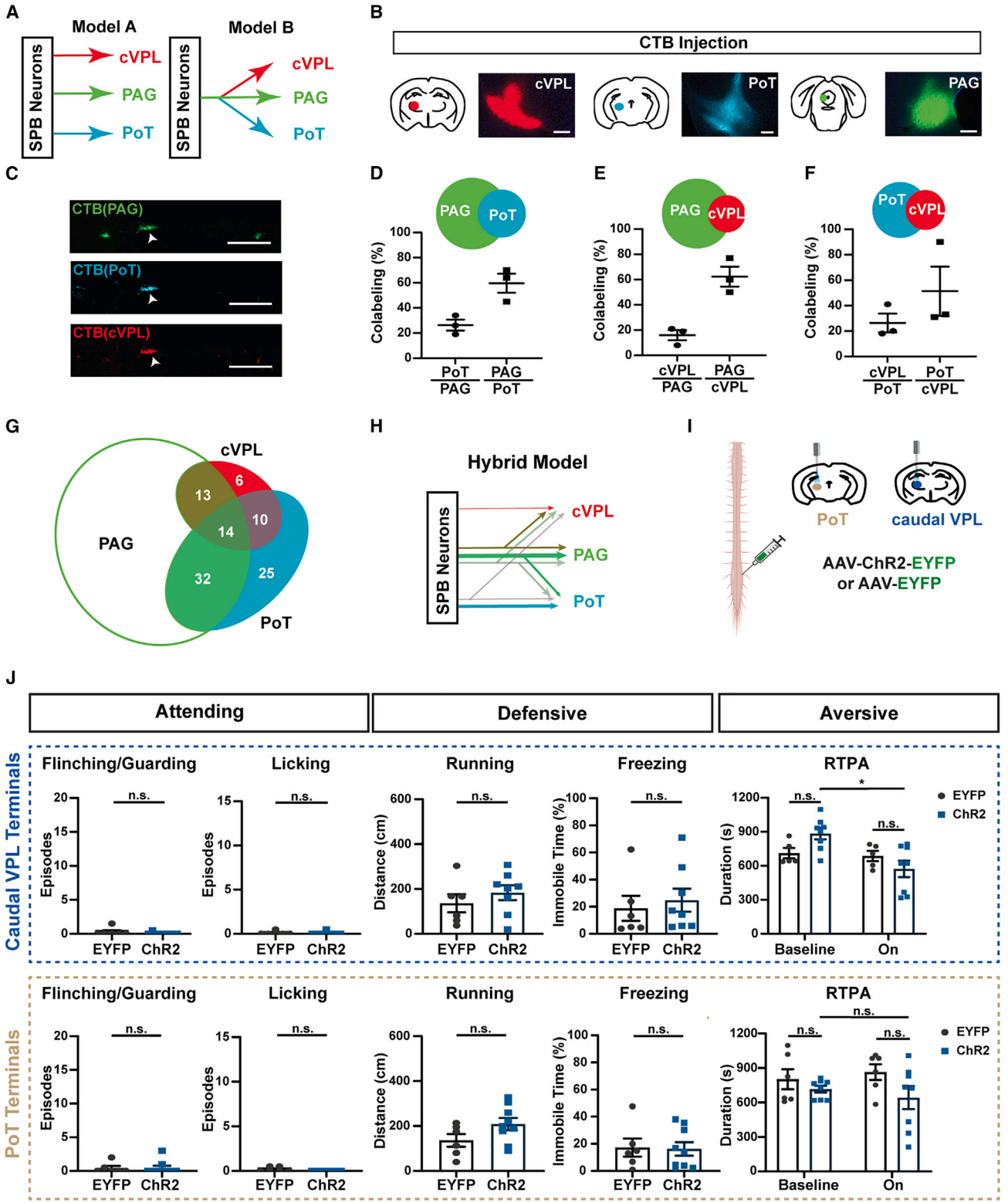

Figure 5. A subset of SPB neurons target the thalamus, but activation of thalamic terminals is not sufficient for nociceptive behaviors

(A) Models illustrating SPB neurons as having collateral targets that are distinct (model A) or shared (model B).

(B) Strategy to retrogradely label spinal neurons projecting to the cVPL, PoT, and PAG simultaneously with fluorophore-conjugated CTBs of different colors. Shown are representative images of CTB injection in the cVPL, PoT, and PAG. Scale bar: 200 μm.

(legend continued on next page)

has shown that nociceptive responses are reduced upon inhibition of either the entire lateral PBN or subsets of neurons therein.[42–44] In keeping with these findings, we observed that chemogenetic inhibition of lumbar SPB neurons significantly reduced formalin-induced licking (Figures 4B and 4C). Although the effect was slight, this diminished formalin response was likely due to decreased nociception because inhibition of SPB neurons had no effect on gross motor performance, as assessed on a rotarod, or on sensorimotor skill, as assessed on a balance beam (Figures 4D and S5A–S5C). In contrast, the inhibition of lumbar SrVPL neurons caused a small but significant increase in the number of foot slips on the balance beam while having no significant effect in the formalin test (Figures 4E–4H) or other simple pain or motor behaviors (Figures S5D–S5N). Because the effects of chemogenetic inhibition of spinal output neurons were modest, we next attempted a cruder approach, inhibiting the entire VPL on the left side, with the hope that this robust manipulation would result in more clear-cut differences (Figure 4I). Upon chemogenetic inhibition of the left VPL, mice showed a side-specific sensorimotor deficit with significantly more instances where the right hindpaw slipped off the narrow balance beam. Again, formalin and rotarod behaviors were unaffected (Figures 4J–4L and S5O–S5Q).

Because we did not observe any obvious effects, at least in simple nociceptive assays, upon manipulation of spinothalamic neurons that ascend in the ventral spinal cord, we instead focused our attention on the spinothalamic neurons that ascend in the lateral spinal cord. Our previous results suggested that SPB neurons, as a population, extend collaterals to three major brain regions: the cVPL and the PoT in the thalamus as well as the PAG in the midbrain. However, whether parallel populations project separately to each target or whether individual neurons project to all three structures remained unclear (Figure 5A). To address this issue, we performed triple retrograde labeling from the PAG, PoT, and cVPL using fluorescent cholera toxin B (CTB) conjugates of different colors and quantified the co-labeling observed in the superficial dorsal horn of the lumbar spinal cord (Figures 5B and 5C). Overall, we observed that more than half of the spinothalamic neurons that ascend in the lateral spinal cord extend collaterals to the PAG (Figures 5D and 5E), consistent with a previous study by Al-Khater and Todd.[13] Moreover, we found that 60% of neurons that project to the PoT also project to the PAG (Figure 5D) and that 60% of neurons that project to the cVPL also project to the PAG (Figure 5E), whereas less than half of the spinothalamic neurons that projected to one thalamic target (e.g., the PoT) also projected to the other (e.g., the cVPL) (Figure 5F). To ensure that this observation was not due to the inadvertent labeling of axons of passage, we used viral tracing to retrogradely label neurons from the PoT. These retrogradely labeled spinothalamic neurons showed synaptic boutons in the PAG, consistent with the idea that the PAG is a *bona fide* target of collateralization (Figures S6A–S6C). Altogether, these results highlight a broad diversity in the patterns of axon collateralization across spinothalamic neurons in the lateral pathway (Figures 5G and 5H).

With the goal of understanding the functional role of the spinothalamic inputs to the PoT and cVPL for nociceptive behaviors, we performed optogenetic stimulation (Figures 5I, S6D, and S6E). However, activation of spinothalamic terminals in either the cVPL or PoT had no obvious effect; mice did not flinch, guard, lick, run, or freeze. In a real-time place aversion test, the effects of optogenetic stimulation were subtle but significant for cVPL stimulation (Figure 5J), which may suggest that this stimulation is somewhat aversive. The major target of neurons in the VPL is the primary somatosensory cortex (S1), whereas the major target of the PoT is the posterior insula (Figures S6F–S6I),[45–47] two cortical structures that are thought to subserve the percept of pain. Nevertheless, when we broadly inhibited either the PoT, insula, or S1 using chemogenetic approaches, these manipulations had no significant effect on formalin-induced nociceptive behaviors (Figures S6J–S6M). In addition, inhibition of the insular cortex did not induce a deficit in simple thermal pain tests either, such as the tail flick and hot plate tests (Figures S6N–S6Q). Thus, activation of spinothalamic terminals in the cVPL or PoT in mice did not elicit any spontaneous nociceptive behaviors, and inhibition of thalamic nuclei (PoT or VPL; see also Figures 4G and 4I) or cortical regions (insula and S1) that are thought to be involved in the percept of pain in humans and other primates did not reduce simple nociceptive behaviors in the formalin test in mice.

We therefore turned our attention to the spinal output neurons that target the PAG and the PBN. In cleared brains from mice in which SPB neurons were labeled from the right side of the lumbar spinal cord, we saw ascending projections that targeted the parabrachial complex on both the ipsilateral (ipsi-PBN) and contralateral (contra-PBN) sides. We also observed many

(C) Representative images of a spinal output neuron in lamina I labeled with different CTBs. An arrow points to a spinal cord neuron that was retrogradely labeled from all three targets: PAG, PoT, and cVPL. Scale bar: 500 μm.
(D) Quantification of colabeling between different lamina I spinal output neurons projecting to the PoT and PAG and the corresponding Venn diagram. Data are mean ± SEM (n = 3 mice).
(E) Quantification of colabeling between different lamina I spinal output neurons projecting to the cVPL and PAG and the corresponding Venn diagram. Data are mean ± SEM (n = 3 mice).
(F) Quantification of colabeling between different lamina I spinal neurons projecting to the PoT and cVPL and the corresponding Venn diagram. Data are mean ± SEM (n = 3 mice).
(G) An Euler diagram representing the relationship between lamina I spinal output neurons projecting to the PAG, PoT, and cVPL. The numbers in the Euler diagram are the percentages of total neurons that were retrogradely labeled from the thalamus (PoT or cVPL).
(H) Summary diagram illustrating a heterogeneous population comprising SPB neurons with both distinct and shared collateral targets.
(I) Strategy to optogenetically activate spinal terminals in the cVPL or PoT.
(J) Optogenetic activation of spinal terminals in the cVPL or PoT did not elicit spontaneous attending behavior, defensive behavior, or real-time place aversion. Data are mean ± SEM with symbols indicating individual mice (n = 5–9 mice).
Two-tailed unpaired t test; n.s, $p > 0.05$. Two-way ANOVA with Sidak correction (I); *$p < 0.05$; n.s., $p > 0.05$.

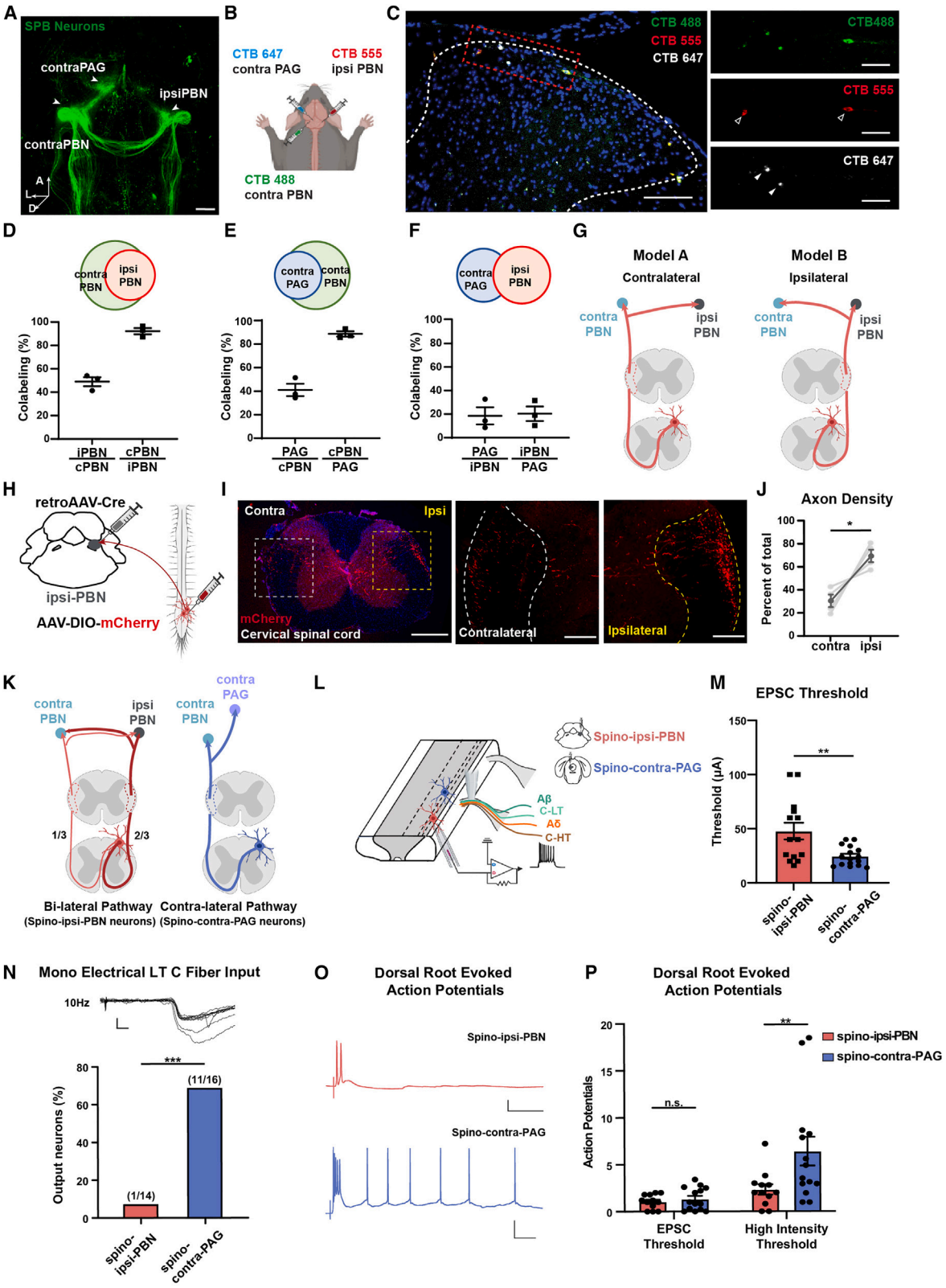

(legend on next page)

axons from SPB neurons that interconnected the parabrachial complex between the ipsilateral and contralateral sides as well as prominent axons that connected the contra-PBN with the contralateral PAG (contra-PAG) (Figure 6A). To understand the anatomy of individual SPB neurons that give rise to this pattern of innervation, we used triple retrograde labeling from the ipsi-PBN, contra-PBN, and contra-PAG and quantified the co-labeling observed in the lumbar spinal cord (Figures 6B and 6C). Almost all SPB neurons that innervated the ipsi-PBN also innervated the contra-PBN, whereas only 50% of neurons that innervated the contra-PBN also innervated the ipsi-PBN (Figure 6D). Similarly, almost all SPB neurons that innervated the contra-PAG also innervated the contra-PBN, whereas only 40% of neurons that innervated the contra-PBN also innervated the contra-PAG (Figure 6E). Finally, when we retrogradely labeled spinal output neurons from either the contra-PAG or the ipsi-PBN, we observed only a 20% overlap (Figure 6F), suggesting that spino-contra-PAG neurons and spino-ipsi-PBN neurons are largely non-overlapping populations.

Because the anterolateral system is typically described as a contralateral pathway that decussates within the spinal cord, our preconceived notion was that innervation of the PBN on the ipsilateral side occurred through a double-crossover pathway (Figure 6G, model A). However, images of SPB neurons in cleared brains showed an abundance of axons that appeared to target the ipsi-PBN via ascending projections on the ipsilateral side (Figure 6G, model B). Granted, some ipsilaterally ascending axons in the lateral pathway have been suggested,[48–50] but the prominence of this ipsilateral projection was nevertheless surprising. To clarify, we selectively labeled right SPB neurons that target the ipsi-PBN with mCherry and measured the degree to which these neurons ascended in the ipsilateral vs. contralateral sides of the spinal cord at cervical levels (Figure 6H). We found that, of neurons that target the ipsi-PBN, approximately 2/3 ascend on the ipsilateral side, whereas 1/3 ascend on the contralateral side (Figures 6I and 6J). Importantly, when we selectively labeled SPB neurons that targeted the ipsi-PBN, these neurons showed few collateral extensions to the PAG or thalamus (Figures S7A–S7C). We also compared the molecular identities of these two populations and found that the fraction of neurons that express *Tacr1* was significantly lower, albeit modestly, among spinal output neurons back-labeled from the ipsi-PBN compared with those back-labeled from the contra-PAG (Figures S7D–S7F). Together, these findings suggested the existence of two distinct populations of SPB neurons: a bilateral pathway that terminates largely in the PBN, which innervates both the contra-PBN and the ipsi-PBN, and a contralateral pathway that extends to the midbrain and beyond, which innervates both the contra-PBN and the contra-PAG (Figure 6K).

To compare the electrophysiological properties of spinal output neurons in the bilateral pathway with those in the contralateral pathway, we performed patch-clamp recordings in spinal cord slices. Both types of output neurons were retrogradely labeled in the same mouse using tracers of different colors, DiI or a retro-AAV encoding enhanced green fluorescent protein (AAVr-EGFP), which were alternately targeted to the ipsi-PBN or contra-PAG (Figure 6L). Although the membrane capacitance was not significantly different between populations, the resting

Figure 6. SPB neurons comprise two major anatomical populations, a bilateral pathway and a contralateral pathway, that have distinct electrophysiological properties

(A) Representative image of a cleared brain showing axons from EYFP-labeled SPB neurons originating in the right spinal cord as seen in a top-down view. Arrows indicate the direction of view. Solid arrows point to three major targets of SPB neurons: the contra-PBN, ipsi-PBN, and contra-PAG. Scale bar: 500 μm.

(B) Strategy to retrogradely label spinal neurons projecting to the contra-PAG, contra-PBN, or ipsi-PBN simultaneously with fluorophore-conjugated CTBs of different colors.

(C) Representative images of spinal neurons labeled by CTB 488 (injected in the contra-PBN), CTB 555 (injected in the ipsi-PBN), or CTB 647 (injected in the contra-PAG). Outlined arrowheads indicate CTB 555-positive neurons, and solid arrowheads indicate CTB 647-positive neurons. Scale bars: 100 μm (left) and 50 μm (right).

(D) Quantification and corresponding Venn diagram of colocalization between spinal cord neurons projecting to the contra-PBN and ipsi-PBN. Data are mean ± SEM, with symbols indicating individual mice (n = 3).

(E) Quantification and corresponding Venn diagram of colocalization between spinal cord neurons projecting to the contra-PBN and contra-PAG. Data are mean ± SEM, with symbols indicating individual mice (n = 3).

(F) Quantification and corresponding Venn diagram of colocalization between spinal cord neurons projecting to the ipsi-PBN and contra-PAG. Data are mean ± SEM, with symbols indicating individual mice (n = 3).

(G) Models illustrating possible axon trajectories of bilateral SPB neurons.

(H) Strategy to selectively label bilateral SPB neurons by targeting the ipsi-PBN neurons.

(I) Representative images of axons from spino-ipsi-PBN neurons in the cervical spinal cord. Scale bars: 500 μm (left) and 200 μm (right).

(J) Quantification of relative axon density of spino-ipsi-PBN neurons that ascend on the contralateral vs. ipsilateral side. Data are mean ± SEM, with light gray lines indicating data from individual mice. Paired Student's t test, *$p < 0.05$.

(K) Summary illustration of two populations of SPB neurons: bilateral pathway (spino-ipsi-PBN neurons) and contralateral pathway (spino-contra-PAG neurons).

(L) Strategy to label and patch clamp spino-ipsi-PBN and spino-contra-PAG neurons with dorsal root stimulation.

(M) Spino-contra-PAG neurons exhibit a significantly lower threshold to evoke monosynaptic EPSCs. Data are mean ± SEM, with symbols indicating individual neurons (n = 14–16 neurons per group). Two-tailed unpaired t test, **$p < 0.01$.

(N) Spino-contra-PAG neurons are significantly more likely to receive monosynaptic input from electrical low-threshold (LT) C fibers compared with spino-ipsi-PBN neurons. Shown at the top are representative traces of EPSCs evoked by 10-Hz dorsal root stimulation. Two-sided Fisher's exact test, ***$p < 0.001$.

(O) Representative traces of action potentials evoked in spino-contra-PAG neurons and spino-ipsi-PBN neurons by maximum-intensity stimulation (300 μA) of the attached dorsal root. Scale bar: 20 mV, 100 ms.

(P) Spino-contra-PAG neurons fire more frequently than spino-ipsi-PBN neurons in response to maximum-intensity stimulation but not in response to lower stimulation intensities equivalent to the EPSC threshold. Data are mean ± SEM (n = 12–14 neurons per group). Two-way ANOVA with Sidak correction; **$p < 0.01$; n.s., $p > 0.05$.

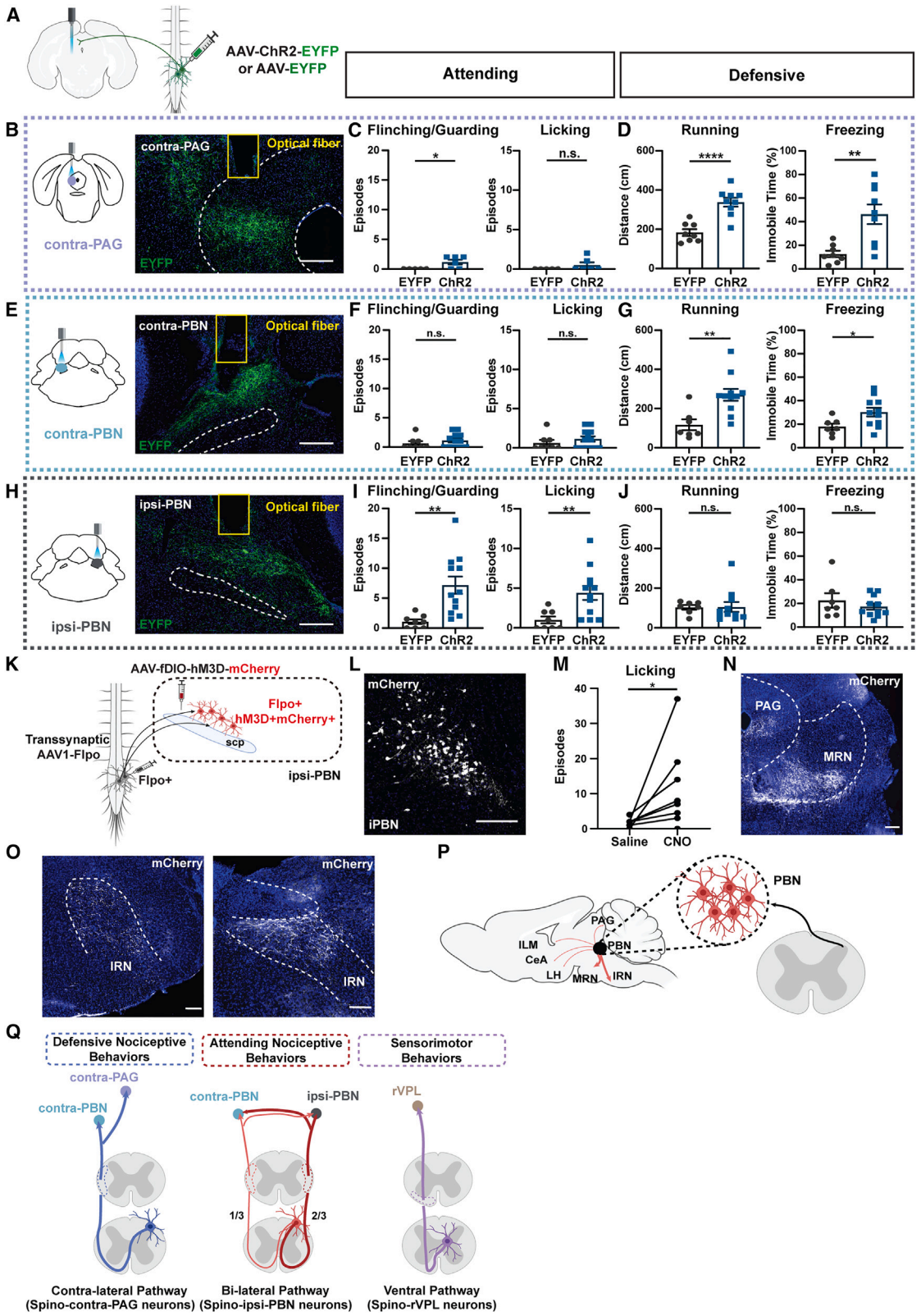

(legend on next page)

membrane potential (V_{rest}) of spino-contra-PAG neurons was slightly more depolarized than that of spino-ipsi-PBN neurons (Figures S7G–S7I). Next, we examined the monosynaptic excitatory postsynaptic currents (EPSCs) that were evoked by electrical stimulation of the dorsal root at different current intensities. We found that spino-contra-PAG neurons showed a significantly lower EPSC threshold than spino-ipsi-PBN neurons (Figure 6M). This is most likely explained by the fact that a significantly higher proportion of spino-contra-PAG neurons (11 of 16) received monosynaptic low-threshold C-fiber input compared with spino-ipsi-PBN neurons (1 of 14) (Figure 6N). Overall, we observed a significant difference in the distribution of monosynaptic primary afferent inputs onto spino-ipsi-PBN vs. spino-contra-PAG neurons ($p = 0.008$, χ^2 test for trend; Figure S7J). These findings suggest that distinct combinations of primary afferents preferentially target these two spinal output neuron types. These data are also in general agreement with prior studies in the immature rat showing that spino-PAG neurons displayed more depolarized resting potentials and a higher prevalence of monosynaptic C-fiber input compared with spino-PBN neurons.[51,52] Finally, we compared the number of action potentials that were evoked from the V_{rest} following electrical stimulation of the dorsal root at different stimulation intensities. At stimulus intensities corresponding to the EPSC threshold, both spinal output neuron types fired an average of one action potential. In contrast, in response to maximum-intensity dorsal root stimulation, spino-contra-PAG neurons fired significantly more action potentials than spino-ipsi-PBN neurons (Figures 6O and 6P). This increase in afferent-evoked action potentials in spino-contra-PAG neurons was reflected in a significantly higher instantaneous firing frequency (Figure S7K) as well as a significantly longer duration of firing (Figure S7L), with many spino-contra-PAG neurons showing persistent after-discharge, as reported in prior studies.[53] In this regard, the pattern of action potential discharge in the spino-PAG cells also resembled the intrinsic burst-firing documented previously in rat spino-PAG neurons.[51] Overall, these recordings reveal that spinal output neurons in the contralateral pathway and the bilateral pathway have distinct electrophysiological properties.

To examine whether the bilateral pathway and the contralateral pathway have distinct functions, we used chemogenetic activation. Pathway selectivity was achieved through the injection of a retroAAV-Cre into either the ipsi-PBN or the contra-PAG, together with Cre-dependent hM3D, into the right spinal cord at the lumbar enlargement (Figure S7M). Activation of the bilateral pathway elicited significant licking of the right hindpaw, whereas activation of the contralateral pathway did not (Figure S7N). To extend these observations, ChR2 was expressed in the right lumbar spinal cord, and optogenetic stimulation was performed at the terminals in either the contra-PAG, the contra-PBN, or the ipsi-PBN (Figure 7A). Optogenetic stimulation of terminals in the contra-PAG elicited robust running behavior that was followed by freezing as soon as the optogenetic stimulation ceased; however, site-directed behaviors such as flinching, licking, or guarding were not observed (Figures 7B–7D and S8A–S8D). Similar results were observed upon optogenetic stimulation of the contra-PBN, where mice displayed defensive behaviors (e.g., running and freezing) but not attending behaviors (e.g., licking and guarding) (Figures 7E–7G and S8E–S8H). In sharp contrast, however, optogenetic stimulation of the ipsi-PBN elicited flinching, guarding, and licking of the right hindpaw but not running or freezing (Figures 7H–7J). These results suggest that activation of spinal output terminals in the contra-PAG or contra-PBN (i.e., components of the contralateral pathway) triggers defensive behaviors, such as running and freezing, whereas activation of spinal output terminals in the ipsi-PBN (i.e., the bilateral pathway) elicits attending behaviors, such as licking and guarding.

The finding that activation of spinomesencephalic terminals in the contra-PAG elicited defensive behaviors fits with the general view that the PAG is involved in mediating motivated behaviors linked to primal emotional responses, such as fear.[54,55] Consistent with this, we found that optogenetic

Figure 7. Optogenetic activation of spinal terminals in the contra-PAG, contra-PBN, and ipsi-PBN induced divergent attending behavior and defensive behavior

(A) Strategy to optogenetically activate terminals of spinal output neurons in different brain loci (contra-PAG, contra-PBN, and ipsi-PBN).

(B) Representative images showing the position of optical fibers in the contra-PAG relative to the spinal cord terminals (EYFP-positive axons). Yellow rectangles represent fiber position. Scale bar: 250 μm.

(C and D) Optogenetic activation of spinal terminals in the contra-PAG induced defensive behavior but not attending behavior. Data are mean ± SEM (n = 8–9 mice per group). Two-tailed unpaired t test; ****$p < 0.0001$, **$p < 0.01$, *$p < 0.05$; n.s., $p > 0.05$. (Bilateral terminals were activated in 3 mice in PAG-ChR2 and 3 mice in PAG-EYFP. Behavioral phenotypes were similar, so data were pooled).

(E) Representative images showing the position of optical fibers in the contra-PBN and corresponding spinal cord terminals (EYFP-positive axons). Yellow rectangles represent fiber position. Scale bar: 250 μm.

(F and G) Optogenetic activation of spinal terminals in the contra-PBN induced defensive behavior but not attending behavior. Data are mean ± SEM (n = 7–11 mice per group). Two-tailed unpaired t test; **$p < 0.01$, *$p < 0.05$; n.s., $p > 0.05$.

(H) Representative images showing the position of optical fibers in the ipsi-PBN and corresponding spinal cord terminals (EYFP-positive axons). Yellow rectangles represent fiber position. Scale bar: 250 μm.

(I and J) Optogenetic activation of spinal terminals in the ipsi-PBN induced attending behavior but not defensive behavior. Data are mean ± SEM (n = 7–11 mice per group). Two-tailed unpaired t test; **$p < 0.01$; n.s., $p > 0.05$.

(K) Strategy to activate neurons in the ipsi-PBN receiving spinal cord input with AAV1 transsynaptic tracing.

(L) One representative image showing neurons in the ipsi-PBN labeled with mCherry. Scale bar: 200 μm.

(M) Activating neurons in the ipsi-PBN receiving spinal cord input induced spontaneous licking behavior quantified 30–60 min after CNO injection (n = 8 mice). Paired Student's t test, *$p < 0.05$.

(N and O) Representative images showing projection targets of neurons in the ipsi-PBN receiving spinal cord input in MRN (N) and IRN (O). Scale bar: 200 μm.

(P) Summary diagram showing projection patterns of neurons in the PBN receiving spinal cord input.

(Q) Summary illustration of three different ascending pathways that mediate different behaviors.

activation of spinal terminals in the contra-PAG or bilaterally in the PBN was aversive (Figures S8I–S8P), consistent with previous reports.[56] In contrast, the idea that activation of SPB terminals in the ipsi-PBN is sufficient for site-directed attending behaviors is not as well established (although this was observed by Deng et al.[56]). These findings suggest that activation of unilateral spinal input to the PBN is sufficient to elicit a patterned motor behavior directed toward the ipsilateral foot. To investigate the underlying neural circuit basis of this phenomenon, we leveraged the transsynaptic properties of AAV1 to capture and express hM3D-mCherry neurons in the ipsi-PBN that are directly innervated by SPB neurons corresponding to the right leg (Figures 7K and 7L). When we chemogenetically activated the PBN neuronal assembly on the ipsilateral side that receives direct SPB input, this manipulation was sufficient to elicit modest licking behavior (Figure 7M). This neuronal ensemble in the ipsi-PBN projected to several regions in the lower brain stem reticular formation, including the midbrain reticular nucleus (MRN) and intermediate reticular nucleus (IRN) (Figures 7N and 7O), which might directly influence motor behaviors,[57–59] as well as several forebrain structures, such as the intralaminar nucleus in the medial thalamus, the central amygdala, and lateral hypothalamus (Figures S8Q and S8R), consistent with previous reports.[56] Taken together, these findings suggest that input from spinal neurons to the ipsilateral side of the PBN is sufficient for attending behavior and raise the possibility that this motor output might be mediated through a descending motor circuit (Figure 7P). When analogous experiments were performed to label neurons in the contra-PAG that receive spinal input, a distinct pattern of projections emerged, including the preoptic area, the lateral hypothalamus, the ventral tegmental area, and the magnocellular reticular nucleus (Figures S8S and S8T), consistent with a different pattern of motor behavior that is observed upon activation of this contralateral pathway.

DISCUSSION

In this study, we examined the logic of spinal output neurons that underlie nociceptive behaviors in mice. We initially targeted the rVPL for retrograde labeling because we found that this region of the thalamus showed the densest spinothalamic input. The selection of this location was somewhat fortuitous because it allowed us to selectively label spinal output neurons that ascend in the ventral aspect of the anterolateral system. In contrast, retrograde labeling of SPB neurons enabled the labeling of neurons that ascend in the lateral aspect of the anterolateral system. Our experiments revealed that these two populations, lateral and ventral, are distinct with respect to their somatic distribution in the spinal cord, axonal anatomy in the brain, and expression of molecular markers. Our studies also revealed that SPB neurons comprised at least two anatomically distinct populations: a bilateral pathway that extends primarily to the PBN and a contralateral pathway that extends collaterals at multiple levels of the neuroaxis, including the PBN, the PAG, and the thalamus. These two populations showed distinct electrophysiological characteristics. Finally, activation of the bilateral pathway elicited attending behaviors (i.e., licking and guarding), whereas activation of the contralateral pathway elicited defensive behaviors (i.e., running and freezing). Thus, our study provides comprehensive insight into the anatomy and functional organization of three anterolateral system output neurons in mice and their roles in acute nociceptive behaviors (Figure 7Q).

In humans, electrical stimulation of the posterior thalamus can evoke pain.[60,61] In contrast, we were unable to evoke any pain behaviors when we activated spinal terminals in the thalamus of mice. Although there are many possible explanations for this apparent discrepancy, we favor the possibility that it reflects the relative paucity of spinothalamic projections that convey nociceptive information to the cortex in mice compared with humans. In contrast, we and others observed that simple nociceptive behaviors characteristic of rodents—flinching, guarding, licking, vocalization, running, freezing, etc.—can be elicited through activation of subcortical structures (PAG and PBN) that may directly engage motor output circuits.[22,56,62] Inhibition of thalamic nuclei and their corresponding cortical targets or even decerebration does not prevent simple nocifensive behaviors such as jumping, avoidance, and even licking (Figures S5 and S6),[63–65] suggesting that simple nocifensive behaviors might be mediated by subcortical nuclei. These findings raise the possibility that simple nociceptive behaviors do not arise simply as consequence of the pain percept and underscore the importance of including more complex affective assays (such as conditioned place preference) in animal studies rather than relying exclusively on nociceptive behaviors that may reflect fixed action patterns.

In this study, distinct axonal targeting allowed us to identify three spinal output types. These axonal trajectories were presumably determined, at least in part, through differential transcription factor expression during embryogenesis. In this regard, it is noteworthy that Phox2a is a transcription factor that is transiently expressed during development in anterolateral tract neurons of the SPB pathway.[21] The Phox2a-cre bacterial artificial chromosome (BAC) transgenic allele marks approximately half of the SPB neurons and appears to preferentially label contralaterally projecting neurons.[66] The Phox2a-labeled neurons have a cell body distribution that closely matches that of SPB neurons reported in our study, including a strong representation in lamina I as well as cell bodies in deeper laminae, including the lateral aspect of lamina V.[67] This transcription factor is particularly interesting because it is related to Phox2b, a critical factor in the development of the autonomic nervous system, highlighting a connection between these sensory input and autonomic output, as noted previously.[9,68]

It is well known that some SPB neurons target the ipsilateral PBN.[69,70] The idea that some noxious information ascends on the ipsilateral side is noteworthy in light of the fact that anterolateral cordotomies, which sever axons on the contralateral side only, are typically unsuccessful for long-term pain relief. Intriguingly, after these surgeries, the pain that re-emerges frequently presents in a mirror-image pattern relative to the original injury.[71,72] We suggest that the ipsilaterally projecting anterolateral pathway provides a neural substrate that might account for this referred pain.

Limitations of the study

We initially predicted that activation of the spinal pathway targeting the VPL—a pathway that is thought to contribute to the

sensory-discriminative component of pain—would elicit some changes in behavior that were at least suggestive of a pain percept,[4,5] but we did not see any obvious effect. There are several limitations to our study that might contribute to this lack of effect. For instance, the degree to which the optogenetic or chemogenetic tools were effective in manipulating cell activity is not fully known. Additionally, considering the relatively low number of fibers within the SrVPL pathway compared with the SPB pathway, particularly at lumbar levels in mice, the impact of manipulating the SrVPL pathway may be subtle. Alternatively, coincident activation of the SrVPL pathway with another pathway may be required for a behavioral response. We note that our manipulations activated many spinothalamic neurons simultaneously, which would be unlikely to occur physiologically. Since these output neurons convey information about distinct somatosensory modalities, there are likely complex interactions between them as well as recurrent circuits and ascending, and descending circuitry, underscoring the need to interpret our data with caution. Finally, our analysis primarily focused on a limited set of acute pain behaviors. Given the well-established role of the cortex in learning, it is plausible that more complex behaviors and/or persistent nociceptive input may be required to unveil the role of spinothalamic neurons in pain-related behaviors in mice.

STAR★METHODS

Detailed methods are provided in the online version of this paper and include the following:

- KEY RESOURCES TABLE
- RESOURCE AVAILABILITY
  - Lead contact
  - Material availability
  - Data and code availability
- EXPERIMENTAL MODEL AND SUBJECT DETAILS
- METHOD DETAILS
  - Viruses
  - Stereotaxic injection and optical fiber implantation
  - Intraspinal injection
  - RNAscope *in situ* hybridization
  - Immunohistochemistry
  - Image acquisition and quantification
  - Whole mouse brain processing and imaging
  - Fos induction
  - Electrophysiology
  - Behavior
  - CNO invoked spontaneous behavior
  - Open field
  - Formalin pain test
  - Hargraves test
  - Cold plantar assay
  - Tail flick
  - Hotplate
  - Rotarod
  - Gait analysis
  - Balance beam
  - Optogenetic behavioral experiments
  - Optogenetic stimulation induced spontaneous behaviors
  - Optogenetic stimulation induced escaping behaviors
  - Real time place aversion
- QUANTIFICATION AND STATISTICAL ANALYSIS

SUPPLEMENTAL INFORMATION

Supplemental information can be found online at https://doi.org/10.1016/j.celrep.2024.113829.

ACKNOWLEDGMENTS

The research reported in this publication was supported by the National Institute of Neurological Disorder and Stroke of the National Institutes of Health under awards R01 NS096705 (to S.E.R.), NS080889 (to M.L.B.), F31 NS134315 (to I.H.B.), F31 NS113371 to (E.K.N.), and T32 NS073548 (to E.K.N. and H.J.S.), as well as the National Institute of Arthritis and Musculoskeletal and Skin Diseases of the National Institutes of Health under award R01AR063772 (to S.E.R.). H.C. (visiting scholar 2019–2022) was supported by Tsinghua University School of Medicine and the Tsinghua Education Foundation North America.

AUTHOR CONTRIBUTIONS

Conceptualization, S.E.R. and H.C.; methodology, H.C., I.H.B., E.K.N., J.L., A.Y.C., H.J.S., K.M.S., M.L.B., and S.E.R.; investigation, H.C., I.H.B., E.K.N., J.L., A.Y.C., H.J.S., K.M.S., M.L.B., and S.E.R.; writing, S.E.R. and H.C. with input from all authors; funding acquisition, S.E.R., M.L.B., I.H.B., E.K.N., and H.J.S.

DECLARATION OF INTERESTS

The authors declare no competing interests.

Received: April 18, 2023
Revised: October 24, 2023
Accepted: February 3, 2024

REFERENCES

1. Hodge, C.J., Jr., and Apkarian, A.V. (1990). The spinothalamic tract. Crit. Rev. Neurobiol. *5*, 363–397.
2. Lenz, F.A., Casey, K.L., Jones, E.G., and Willis, W.D. (2010). The Human Pain System: Experimental and Clinical Perspectives (Cambridge University Press).
3. Basbaum, A. (2022). History of Spinal Cord "Pain" Pathways Including the Pathways Not Taken. Front. Pain Res. *3*, 910954.
4. Willis, W., and Westlund, K. (1997). Neuroanatomy of the pain system and of the pathways that modulate pain. J. Clin. Neurophysiol. *14*, 2. official publication of the American Electroencephalographic Society.
5. Almeida, T.F., Roizenblatt, S., and Tufik, S. (2004). Afferent pain pathways: a neuroanatomical review. Brain Res. *1000*, 40–56.
6. Craig, A.D. (2004). Lamina I, but not lamina V, spinothalamic neurons exhibit responses that correspond with burning pain. J. Neurophysiol. *92*, 2604–2609.
7. Craig, A.D.B. (2003). Pain mechanisms: labeled lines versus convergence in central processing. Annu. Rev. Neurosci. *26*, 1–30.
8. Craig, A.D., Bushnell, M.C., Zhang, E.-T., and Blomqvist, A. (1994). A thalamic nucleus specific for pain and temperature sensation. Nature *372*, 770–773.
9. Craig, A.D. (2003). Interoception: the sense of the physiological condition of the body. Curr. Opin. Neurobiol. *13*, 500–505.

10. Blomqvist, A., Zhang, E.-T., and Craig, A.D. (2000). Cytoarchitectonic and immunohistochemical characterization of a specific pain and temperature relay, the posterior portion of the ventral medial nucleus, in the human thalamus. Brain *123 Pt 3*, 601–619.

11. Dum, R.P., Levinthal, D.J., and Strick, P.L. (2009). The spinothalamic system targets motor and sensory areas in the cerebral cortex of monkeys. J. Neurosci. *29*, 14223–14235.

12. Polgár, E., Wright, L.L., and Todd, A.J. (2010). A quantitative study of brainstem projections from lamina I neurons in the cervical and lumbar enlargement of the rat. Brain Res. *1308*, 58–67.

13. Al-Khater, K.M., and Todd, A.J. (2009). Collateral projections of neurons in laminae I, III, and IV of rat spinal cord to thalamus, periaqueductal gray matter, and lateral parabrachial area. J. Comp. Neurol. *515*, 629–646.

14. Hylden, J.L., Anton, F., and Nahin, R.L. (1989). Spinal lamina I projection neurons in the rat: collateral innervation of parabrachial area and thalamus. Neuroscience *28*, 27–37.

15. Spike, R.C., Puskár, Z., Andrew, D., and Todd, A.J. (2003). A quantitative and morphological study of projection neurons in lamina I of the rat lumbar spinal cord. Eur. J. Neurosci. *18*, 2433–2448.

16. Almarestani, L., Waters, S.M., Krause, J.E., Bennett, G.J., and Ribeiro-da-Silva, A. (2007). Morphological characterization of spinal cord dorsal horn lamina I neurons projecting to the parabrachial nucleus in the rat. J. Comp. Neurol. *504*, 287–297.

17. Han, Z.-S., Zhang, E.-T., and Craig, A.D. (1998). Nociceptive and thermoreceptive lamina I neurons are anatomically distinct. Nat. Neurosci. *1*, 218–225.

18. Bester, H., Chapman, V., Besson, J.-M., and Bernard, J.F. (2000). Physiological properties of the lamina I spinoparabrachial neurons in the rat. J. Neurophysiol. *83*, 2239–2259.

19. Browne, T.J., Smith, K.M., Gradwell, M.A., Iredale, J.A., Dayas, C.V., Callister, R.J., Hughes, D.I., and Graham, B.A. (2021). Spinoparabrachial projection neurons form distinct classes in the mouse dorsal horn. Pain *162*, 1977–1994.

20. Alsulaiman, W.A.A., Quillet, R., Bell, A.M., Dickie, A.C., Polgár, E., Boyle, K.A., Watanabe, M., Roome, R.B., Kania, A., Todd, A.J., and Gutierrez-Mecinas, M. (2021). Characterisation of lamina I anterolateral system neurons that express Cre in a Phox2a-Cre mouse line. Sci. Rep. *11*, 17912. https://doi.org/10.1038/s41598-021-97105-w.

21. Roome, R.B., Bourojeni, F.B., Mona, B., Rastegar-Pouyani, S., Blain, R., Dumouchel, A., Salesse, C., Thompson, W.S., Brookbank, M., Gitton, Y., et al. (2020). Phox2a defines a developmental origin of the anterolateral system in mice and humans. Cell Rep. *33*, 108425.

22. Choi, S., Hachisuka, J., Brett, M.A., Magee, A.R., Omori, Y., Iqbal, N.-u.-A., Zhang, D., DeLisle, M.M., Wolfson, R.L., Bai, L., et al. (2020). Parallel ascending spinal pathways for affective touch and pain. Nature *587*, 258–263.

23. Huang, T., Lin, S.-H., Malewicz, N.M., Zhang, Y., Zhang, Y., Goulding, M., LaMotte, R.H., and Ma, Q. (2019). Identifying the pathways required for coping behaviours associated with sustained pain. Nature *565*, 86–90.

24. Wercberger, R., and Basbaum, A.I. (2019). Spinal cord projection neurons: a superficial, and also deep analysis. Curr. Opin. Physiol. *11*, 109–115.

25. Ma, Q. (2022). A functional subdivision within the somatosensory system and its implications for pain research. Neuron.

26. Wang, L.-H., Ding, W.-Q., and Sun, Y.-G. (2022). Spinal ascending pathways for somatosensory information processing. Trends Neurosci.

27. Cameron, D., Polgár, E., Gutierrez-Mecinas, M., Gomez-Lima, M., Watanabe, M., and Todd, A.J. (2015). The organisation of spinoparabrachial neurons in the mouse. Pain *156*, 2061–2071.

28. Kitamura, T., Yamada, J., Sato, H., and Yamashita, K. (1993). Cells of origin of the spinoparabrachial fibers in the rat: A study with fast blue and WGA-HRP. J. Comp. Neurol. *328*, 449–461.

29. Willis, W.D., Jr., Zhang, X., Honda, C.N., and Giesler, G.J., Jr. (2001). Projections from the marginal zone and deep dorsal horn to the ventrobasal nuclei of the primate thalamus. Pain *92*, 267–276.

30. Moreno-López, Y., Martínez-Lorenzana, G., Condés-Lara, M., and Rojas-Piloni, G. (2013). Identification of oxytocin receptor in the dorsal horn and nociceptive dorsal root ganglion neurons. Neuropeptides *47*, 117–123.

31. Davidson, S., Truong, H., and Giesler, G.J., Jr. (2010). Quantitative analysis of spinothalamic tract neurons in adult and developing mouse. J. Comp. Neurol. *518*, 3193–3204.

32. Burstein, R., Dado, R.J., and Giesler, G.J., Jr. (1990). The cells of origin of the spinothalamic tract of the rat: a quantitative reexamination. Brain Res. *511*, 329–337.

33. Häring, M., Zeisel, A., Hochgerner, H., Rinwa, P., Jakobsson, J.E.T., Lönnerberg, P., La Manno, G., Sharma, N., Borgius, L., Kiehn, O., et al. (2018). Neuronal atlas of the dorsal horn defines its architecture and links sensory input to transcriptional cell types. Nat. Neurosci. *21*, 869–880.

34. Lu, G.-W., and Willis, W.D. (1999). Branching and/or collateral projections of spinal dorsal horn neurons. Brain Res. Rev. *29*, 50–82.

35. Francis, J.T., Xu, S., and Chapin, J.K. (2008). Proprioceptive and cutaneous representations in the rat ventral posterolateral thalamus. J. Neurophysiol. *99*, 2291–2304.

36. Apkarian, A.V., and Hodge, C.J. (1989). Primate spinothalamic pathways: II. The cells of origin of the dorsolateral and ventral spinothalamic pathways. J. Comp. Neurol. *288*, 474–492.

37. Applebaum, A.E., Beall, J.E., Foreman, R.D., and Willis, W.D. (1975). Organization and receptive fields of primate spinothalamic tract neurons. J. Neurophysiol. *38*, 572–586.

38. Jones, M.W., Apkarian, A.V., Stevens, R.T., and Hodge, C.J., Jr. (1987). The spinothalamic tract: an examination of the cells of origin of the dorsolateral and ventral spinothalamic pathways in cats. J. Comp. Neurol. *260*, 349–361.

39. McMahon, S.B., and Wall, P.D. (1983). A system of rat spinal cord lamina 1 cells projecting through the contralateral dorsolateral funiculus. J. Comp. Neurol. *214*, 217–223.

40. Muñoz, A., Muñoz, M., Gonź lez, A., and Ten Donkelaar, H. (1997). Spinal ascending pathways in amphibians: cells of origin and main targets. J. Comp. Neurol. *378*, 205–228.

41. Kennard, M.A. (1954). The course of ascending fibers in the spinal cord of the cat essential to the recognition of painful stimuli. J. Comp. Neurol. *100*, 511–524.

42. Barik, A., Sathyamurthy, A., Thompson, J., Seltzer, M., Levine, A., and Chesler, A. (2021). A spinoparabrachial circuit defined by Tacr1 expression drives pain. Elife *10*, e61135.

43. Yang, H., de Jong, J.W., Cerniauskas, I., Peck, J.R., Lim, B.K., Gong, H., Fields, H.L., and Lammel, S. (2021). Pain modulates dopamine neurons via a spinal–parabrachial–mesencephalic circuit. Nat. Neurosci. *24*, 1402–1413.

44. Chiang, M.C., Nguyen, E.K., Canto-Bustos, M., Papale, A.E., Oswald, A.-M.M., and Ross, S.E. (2020). Divergent neural pathways emanating from the lateral parabrachial nucleus mediate distinct components of the pain response. Neuron *106*, 927–939.e5.

45. Gauriau, C., and Bernard, J.-F. (2004). Posterior triangular thalamic neurons convey nociceptive messages to the secondary somatosensory and insular cortices in the rat. J. Neurosci. *24*, 752–761.

46. Gehrlach, D.A., Weiand, C., Gaitanos, T.N., Cho, E., Klein, A.S., Hennrich, A.A., Conzelmann, K.-K., and Gogolla, N. (2020). A whole-brain connectivity map of mouse insular cortex. Elife *9*, e55585.

47. Yamawaki, N., Raineri Tapies, M.G., Stults, A., Smith, G.A., and Shepherd, G.M. (2021). Circuit organization of the excitatory sensorimotor loop through hand/forelimb S1 and M1. Elife *10*, e66836.

48. Nahin, R.L., Madsen, A.M., and Giesler, G.J., Jr. (1986). Funicular location of the ascending axons of neurons adjacent to the spinal cord central canal in the rat. Brain Res. *384*, 367–372.

49. Hylden, J.L., Hayashi, H., and Bennett, G.J. (1986). Lamina I spinomesencephalic neurons in the cat ascend via the dorsolateral funiculi. Somatosens. Res. *4*, 31–41.

50. Noordenbos, W., and Wall, P.D. (1976). Diverse sensory functions with an almost totally divided spinal cord. A case of spinal cord transection with preservation of part of one anterolateral quadrant Pain *2*, 185–195.

51. Ruscheweyh, R., Ikeda, H., Heinke, B., and Sandkühler, J. (2004). Distinctive membrane and discharge properties of rat spinal lamina I projection neurones in vitro. J. Physiol. *555*, 527–543.

52. Dahlhaus, A., Ruscheweyh, R., and Sandkühler, J. (2005). Synaptic input of rat spinal lamina I projection and unidentified neurones in vitro. J. Physiol. *566*, 355–368.

53. Li, J., Serafin, E.K., and Baccei, M.L. (2022). Intrinsic and synaptic properties of adult mouse spino-PAG neurons and the influence of neonatal tissue damage. Pain *10*, 1097.

54. Lefler, Y., Campagner, D., and Branco, T. (2020). The role of the periaqueductal gray in escape behavior. Curr. Opin. Neurobiol. *60*, 115–121.

55. Deng, H., Xiao, X., and Wang, Z. (2016). Periaqueductal gray neuronal activities underlie different aspects of defensive behaviors. J. Neurosci. *36*, 7580–7588.

56. Deng, J., Zhou, H., Lin, J.-K., Shen, Z.-X., Chen, W.-Z., Wang, L.-H., Li, Q., Mu, D., Wei, Y.-C., Xu, X.-H., and Sun, Y.G. (2020). The parabrachial nucleus directly channels spinal nociceptive signals to the intralaminar thalamic nuclei, but not the amygdala. Neuron *107*, 909–923.e6.

57. McElvain, L.E., Friedman, B., Karten, H.J., Svoboda, K., Wang, F., Deschênes, M., and Kleinfeld, D. (2018). Circuits in the rodent brainstem that control whisking in concert with other orofacial motor actions. Neuroscience *368*, 152–170.

58. Ferreira-Pinto, M.J., Ruder, L., Capelli, P., and Arber, S. (2018). Connecting circuits for supraspinal control of locomotion. Neuron *100*, 361–374.

59. Lee, A.M., Hoy, J.L., Bonci, A., Wilbrecht, L., Stryker, M.P., and Niell, C.M. (2014). Identification of a brainstem circuit regulating visual cortical state in parallel with locomotion. Neuron *83*, 455–466.

60. Lenz, F.A., Seike, M., Richardson, R.T., Lin, Y.C., Baker, F.H., Khoja, I., Jaeger, C.J., and Gracely, R.H. (1993). Thermal and pain sensations evoked by microstimulation in the area of human ventrocaudal nucleus. J. Neurophysiol. *70*, 200–212.

61. Ohara, S., and Lenz, F.A. (2003). Medial lateral extent of thermal and pain sensations evoked by microstimulation in somatic sensory nuclei of human thalamus. J. Neurophysiol. *90*, 2367–2377.

62. Rodriguez, E., Sakurai, K., Xu, J., Chen, Y., Toda, K., Zhao, S., Han, B.-X., Ryu, D., Yin, H., Liedtke, W., and Wang, F. (2017). A craniofacial-specific monosynaptic circuit enables heightened affective pain. Nat. Neurosci. *20*, 1734–1743.

63. Barik, A., Thompson, J.H., Seltzer, M., Ghitani, N., and Chesler, A.T. (2018). A brainstem-spinal circuit controlling nocifensive behavior. Neuron *100*, 1491–1503.e3.

64. Gehrlach, D.A., Dolensek, N., Klein, A.S., Roy Chowdhury, R., Matthys, A., Junghänel, M., Gaitanos, T.N., Podgornik, A., Black, T.D., Reddy Vaka, N., et al. (2019). Aversive state processing in the posterior insular cortex. Nat. Neurosci. *22*, 1424–1437.

65. Yahiro, T., Kataoka, N., Nakamura, Y., and Nakamura, K. (2017). The lateral parabrachial nucleus, but not the thalamus, mediates thermosensory pathways for behavioural thermoregulation. Sci. Rep. *7*, 5031.

66. Alsulaiman, W.A.A., Quillet, R., Bell, A.M., Dickie, A.C., Polgár, E., Boyle, K.A., Watanabe, M., Roome, R.B., Kania, A., Todd, A.J., and Gutierrez-Mecinas, M. (2021). Characterisation of lamina I anterolateral system neurons that express Cre in a Phox2a-Cre mouse line. Sci. Rep. *11*, 17912.

67. Kókai, É., Alsulaiman, W.A., Dickie, A.C., Bell, A.M., Goffin, L., Watanabe, M., Gutierrez-Mecinas, M., and Todd, A.J. (2022). Characterisation of deep dorsal horn projection neurons in the spinal cord of the Phox2a:: Cre mouse line. Mol. Pain *18*. 17448069221119614.

68. Craig, A.D. (2002). How do you feel? Interoception: the sense of the physiological condition of the body. Nat. Rev. Neurosci. *3*, 655–666.

69. Blomqvist, A., Ma, W., and Berkley, K.J. (1989). Spinal input to the parabrachial nucleus in the cat. Brain Res. *480*, 29–36.

70. Cechetto, D.F., Standaert, D.G., and Saper, C.B. (1985). Spinal and trigeminal dorsal horn projections to the parabrachial nucleus in the rat. J. Comp. Neurol. *240*, 153–160.

71. Nagaro, T., Adachi, N., Tabo, E., Kimura, S., Arai, T., and Dote, K. (2001). New pain following cordotomy: clinical features, mechanisms, and clinical importance. J. Neurosurg. *95*, 425–431.

72. Bowsher, D. (1988). Contralateral mirror-image pain following anterolateral cordotomy. Pain *33*, 63–65.

73. Powell, J.M., Plummer, N.W., Scappini, E.L., Tucker, C.J., and Jensen, P. (2018). DEFiNE: a method for enhancement and quantification of fluorescently labeled axons. Front. Neuroanat. *12*, 117.

74. Park, Y.-G., Sohn, C.H., Chen, R., McCue, M., Yun, D.H., Drummond, G.T., Ku, T., Evans, N.B., Oak, H.C., Trieu, W., et al. (2019). Protection of tissue physicochemical properties using polyfunctional crosslinkers. Nat. Biotechnol. *37*, 73–83.

75. Kim, S.-Y., Cho, J.H., Murray, E., Bakh, N., Choi, H., Ohn, K., Ruelas, L., Hubbert, A., McCue, M., Vassallo, S.L., et al. (2015). Stochastic electrotransport selectively enhances the transport of highly electromobile molecules. Proc. Natl. Acad. Sci. USA *112*, E6274–E6283.

76. Li, J., Kritzer, E., Craig, P.E., and Baccei, M.L. (2015). Aberrant synaptic integration in adult lamina I projection neurons following neonatal tissue damage. J. Neurosci. *35*, 2438–2451.

77. Ben-Shaul, Y. (2017). OptiMouse: a comprehensive open source program for reliable detection and analysis of mouse body and nose positions. BMC Biol. *15*. 41-22.

STAR★METHODS

KEY RESOURCES TABLE

REAGENT or RESOURCE	SOURCE	IDENTIFIER
Antibodies		
Donkey anti-rabbit (IgG) Alexa Fluor 555 secondary antibody	ThermoFisher	A-31572
Donkey anti-chicken (IgG) Alexa Fluor 488 secondary antibody	Jackson ImmunoResearch	703-035-155
Donkey anti-rabbit (IgG) Alexa Fluor 647 secondary antibody	ThermoFisher	A-31573
Goat anti-Chicken IgY (H + L) Secondary Antibody, Alexa Fluor™ 555	ThermoFisher	A-21437
Chicken anti-GFP	Aves Laboratory	GFP-1020; RRID AB_2307313
Rabbit-anti Fos	Cell Signaling Technology	2250S; RRID AB_2247211
Chicken anti-RFP	Rockland	600-901-379; RRID AB_10703148
Rabbit anti-RFP	Rockland	600-401-379; RRID AB_10703148
Bacterial and virus strains		
AAVrg-hSyn-EGFP	Bryan Roth	Addgene, 50465-AAVrg
AAVrg-CAG-tdTomato	Edward Boyden	Addgene, 59462-AAVrg
AAV8-hSyn-EGFP	Bryan Roth	Addgene,50465-AAV8
pENN.AAVrg-hSyn.HI-eGFP-Cre-WPRE.SV40	James M. Wilson	Addgene,105540-AAVrg
AAVrg-EF1a-Cre	Karl Deisseroth	Addgene,55636-AAVrg
pENN.AAVrg-hSyn-Cre-WPRE.hGH	James M. Wilson	Addgene,105553-AAVrg
AAVrg-EF1a-Flpo	Karl Deisseroth	Addgene,100187-AAVrg
AAV2-Ef1a-DIO-EYFP	Karl Deisseroth	Addgene,27056-AAV2
AAV8-CAG-tdTomato	Edward Boyden	Addgene,59462-AAV8
AAV8-hSyn-DIO-hM3D(Gq)-mCherry	Bryan Roth	Addgene,44361-AAV8
AAV8-hSyn-DIO-mCherry	Bryan Roth	Addgene,50459-AAV8
AAV2-hSyn-DIO-hM4D(Gi)-mCherry	Bryan Roth	Addgene,44362-AAV2
AAV2-hsyn-DIO-mCherry	Bryan Roth	Addgene,50459-AAV2
AAV5-CaMKIIa-hM4D(Gi)-mCherry	Bryan Roth	Addgene,50477-AAV5
AAV5-CaMKIIa-mCherry	Karl Deisseroth	Addgene,114469-AAV5
pENN.AAV1-hSyn-Cre-WPRE.hGH	James M. Wilson	Addgene,105553-AAV1
AAV1-EF1a-Flpo	Karl Deisseroth	Addgene,55637-AAV1
AAV2-hSyn-EGFP	Bryan Roth	Addgene,50465-AAV2
AAV1.hSyn.HI.eGFP-Cre.WPRE.SV40	James M. Wilson	Addgene,105540-AAV1
AAV2.hSyn.hChR2(H134R).eYFP.WPREpA	UNC Vector Core	N/A
AAV8-EF1a-fDIO-Gq-DREADD-mCherry	Stanford GVVC	AAV-170
Chemicals, peptides, and recombinant proteins		
Clozapine-N-oxide	Tocris	34233-69-7
Cholera toxin subunit B (Recombinant), Alexa Fluor 647	ThermoFisher	C22843
Cholera toxin subunit B (Recombinant), Alexa Fluor 488	ThermoFisher	C22841
Cholera toxin subunit B (Recombinant), Alexa Fluor 555	ThermoFisher	C34778
Paraformaldehye	Sigma Aldrich	30525-89-4
Formalin	Sigma Aldrich	HT501128

(*Continued on next page*)

Continued

REAGENT or RESOURCE	SOURCE	IDENTIFIER
Critical commercial assays		
RNAscope® Multiplex Fluorescent Reagent Kit	ACD	320851
RNAscope® Multiplex Fluorescent Reagent Kit v2	ACD	323100
DAPI	ACD	320858
3-plex positive control probe	ACD	320881
3-plex negative control probe	ACD	320871
Tacr1	ACD	C1-428781
Lypd1	ACD	C3-318361
Tac1	ACD	C2-410351
Penk	ACD	C1-318761
CCK	ACD	C1-461721
Slc17a6	ACD	C1-319171
Gpr83	ACD	C1-317431
Experimental models: Organisms/strains		
C57BL6	Charles River	027
Software and algorithms		
MATLAB	Mathworks	https://www.mathworks.com
Fiji/ImageJ	National Institute of Health, USA	https://imagej.net
Original code	This manuscript	https://doi.org/10.5281/zenodo.10599967

RESOURCE AVAILABILITY

Lead contact

Further information and requests for resources and reagents should be directed to and will be fulfilled by the corresponding authors and Lead Contact, Dr. Sarah E. Ross (saross@pitt.edu).

Material availability

This study did not generate new unique reagents.

Data and code availability

- All behavior, imaging and electrophysiology data included in this paper will be shared by the lead contact upon request.
- Custom-written MATLAB code has been deposited at Zenodo and is publicly available. DOIs are listed in the key resources table.
- Any additional information required to reanalyze the data reported in this paper is available from the lead contact upon request.

EXPERIMENTAL MODEL AND SUBJECT DETAILS

For the majority of experiments, mice were housed and handled in accordance with guidelines approved by the Institutional Animal Care and Use Committee of the University of Pittsburgh. Mice were given free access to food and water with a 12h light/dark cycle. All mice used are wild type C57BL/6 mice purchased from Charles River (Cat#027). Male and female mice at the age of 6–20 weeks were used in approximately equal numbers for all experiments. No obvious differences were observed between males and females, although experiments were not powered to detect sex differences.

In electrophysiological experiments (Figures 6L–6P and S7G–S7K), mice were housed in accordance with animal welfare guidelines outlined by the Institutional Animal Care and Use Committee at the University of Cincinnati. Adult (P63–84) male and female wild-type FVB mice were used.

METHOD DETAILS

Viruses

The following viruses were used for these experiments: AAVrg-hSyn-EGFP (Addgene#50465), AAVrg-CAG-tdTomato (Addgene#59462), pENN.AAVrg-hSyn.HI-eGFP-Cre-WPRE.SV40 (Addgene#105540), AAV1.hSyn.HI.eGFP-Cre.WPRE.SV40 (Addgene#105540), AAVrg-EF1a-Cre

(Addgne#55636), AAVrg-EF1a-Flpo (Addgne#100187), pENN.AAVrg-hSyn-Cre-WPRE.hGH (Addgene#105553), AAV8-hSyn-EGFP (Addgene# 50465), AAV8-hSyn-DIO-hM3D(Gq)-mCherry (Addgene# 44361), AAV8-hSyn-DIO-mCherry (Addgene# 50459), AAV2-hSyn-DIO-hM4D(Gi)-mCherry (Addgene#44362), AAV2-hSyn-DIO-mCherry (Addgene# 50459), AAV2-Ef1a-DIO-EYFP (Addgene#27056), AAV8-CAG-tdTomato (Addgene#59462), AAV1-EF1a-Flpo (Addgene# 55637), AAV2-hSyn-EGFP (Addgene#50465), AAV5-CaMKIIa-hM4D(Gi)-mCherry (Addgene#50477), AAV5-CaMKIIa-mCherry (Addgene#114469), AAV2.hSyn.hChR2(H134R).eYFP.WPREpA (UNC Vector Core), AAV8-EF1a-fDIO-mCherry-WPRE (Stanford GVVC-AAV-155) and AAV8-EF1a-fDIO-Gq-DREADD-mCherry(Stanford GVVC-AAV-170).

Stereotaxic injection and optical fiber implantation

Mice were placed on a standard stereotaxic frame with heads fixed by ear bars. During surgery, mice were kept anesthetized with isoflurane (1–2%) using a vaporizer. An incision was made to expose the skull. 3% Hydrogen peroxide was used to make the suture clearer. The skull was aligned and burr holes were made by a dental drill (MA Ford, #87). 200–400 nL of virus was injected by a pulled glass pipette with a nano injector (Drummond Scientific Company) at the speed of 2 nL/s. The glass pipette was kept at the injection site 3 min after injection. Afterward, the pipette was pulled up and left 0.25 mm higher than the injection site for another 3 min. The incision was enclosed by 5-0 Vicryl suture and mice were treated with ketofen.

For optical fiber implants, customer made fibers (Thor Labs: 1.25 mm ceramic ferrule 230 mm diameter) were implanted and fixed by dental cement and Vetbond (3M). The injection coordinates were listed as follows: rVPL: −1.25–1.5 mm AP, 1.8–1.9 mm ML, 3.55 mm DV; cVPL: −2.2–2.4 mm AP, 1.9 mm ML, 3.55 mm DV; PoT: −2.9–3.1 mm AP, 1.7 mm ML, 3.3 mm DV; PAG: −4.6–4.8 mm AP, 0.6 mm ML, 2.5–2.65 mm DV; PBN: −5.05–5.2 mm AP, 1.3 mm ML, 3.43 mm DV. Mice were treated with ketofen. Mice were allowed to recover for at least 4 weeks before behavioral experiments. For retrograde tracing, tissue collection was conducted 10 days after surgery for CTB-injected mice and 3 weeks after surgery for retroAAV-injected mice.

For electrophysiological experiments, mice (7–8 weeks old) were anesthetized with a mixture of ketamine (90 mg/kg) and xylazine (10 mg/kg) given via intraperitoneal injection and secured in a stereotaxic apparatus. A single injection of FAST DiI oil (100 nL; 2.5 mg/mL) was administered into the right PAG using a Hamilton micro-syringe (62RN; 2.5 μL volume) equipped with a 28-gauge removable needle. The following stereotaxic coordinates were used (in mm; relative to bregma): 3.8–4.0 caudal, 0.4–0.5 lateral and 3.5–3.7 ventral. The same mice also received injections of AAV1.hSyn.HI.eGFP-Cre.WPRE.SV40 (400 nL) into the left parabrachial nucleus (PB) using the following coordinates (in mm; relative to bregma): 4.8–5.0 caudal, 1.0–1.3 lateral and 4.1–4.5 ventral. Alternatively, mice received an injection of AAV1.hSyn.HI.eGFP-Cre.WPRE.SV40 (300 nL) into the right PAG combined with an injection of FAST DiI (120 nL) into the left PB. Mice were allowed to recover for 14–21 days following the dual injections before experiments.

Intraspinal injection

Mice were anesthetized by 1–2% isoflurane with a vaporizer. Furs of back were shaved to get a cleaner surgery view. An incision was made along the rostral-caudal axis. Muscle was cut off to expose intrathecal spaces corresponding to L2-L6. For cervical spinal cord injection, intrathecal spaces corresponding to C5-C8 were exposed. Two injections were made at two intrathecal spaces (above and below C6 and T13 vertebrae). 600–800 nL virus was injected at a depth of 300–500 μm below the surface of spinal cord at a rate of 5 nL/s with pulled glass pipettes. The needle was left at the injection site for 3 min after injection. The incision was sutured after surgery and mice were treated with ketofen postoperatively.

RNAscope *in situ* hybridization

Mice were anesthetized with 100 mg/kg ketamine and 10 mg/kg xylazine, transcardially perfused with 20–30 mL PBS, and then with 40 mL freshly made 4% paraformaldehyde. Lumbar spinal cord was collected and post fixed for 2 h. The spinal cord was incubated in 30% sucrose for 2 days and embedded with OCT compound. 16–18 μm slices were collected on glass slides with cryosection. mRNA transcripts were detected by RNAscope Multiplex Fluorescent v2 Assay (Advanced Cell Diagnostics # 323100) following the manufacturer's instructions. IHC was conducted after ISH to amplify the tdTomato or EYFP fluorescent based on the protocol provided by Advance Cell Diagnostics (RNAscope Multiplex Fluorescent Assay Combined with Immunofluorescent Technical Note). The probes used include Slc17a6, Tacr1, Lypd1, Tac1, GPR83, and CCK.

Immunohistochemistry

Mice were anesthetized with 100 mg/kg ketamine and 10 mg/kg xylazine, and perfused with first PBS and then ice-cold 4% paraformaldehyde. The brain and spinal cord were collected, incubated in 4% paraformaldehyde overnight and then 30% sucrose for two days with gentle shaking. 40–60 μm slices of brain and 16–18 μm slices of spinal cord were collected with a cryostat (Leica). Brain sections were collected in 12-well cell culture plates with PBS and spinal cord sections were collected on glass slides directly. Free floating slices were stored in 4°C PBS and glass mounted slices were kept in a −80°C freezer. Before staining, spinal cord slices were taken out of the freezer at least 1 h in advance to make sure slices recover to room temperature. For staining, tissues were first washed with PBST (0.3% PBST) three times for 10 min each for free floating slices and 5 min each for spinal cord slices. Slices were incubated in blocking serum (10% donkey serum in 0.3%PBST) (Jackson ImmunoResearch, 017-000-121) at room temperature for 1 h and then primary antibody (diluted in 5% donkey serum) overnight at 4°C, washed 3 times in 0.3% PBST for 5 min each, incubated in secondary antibody (diluted in 5% donkey serum) at room temperature for 2 h (brain free floating slices) or 1 h (slice

mounted spinal cord slices) and then 1:10000 Hoechst (ThermoFisher, 1:10K). Lastly, slices were washed 3 times for 5 min each in PBS and mounted. Primary antibodies used include rabbit anti-c-Fos (1:1000, Cell signaling), chicken anti-GFP (1:1000, Aves Labs), rabbit anti-RFP (1:1000, Rockland), and chicken anti-RFP (1:1000, Rockland). Secondary antibodies used included donkey anti-rabbit Alexa Fluor 555, goat anti-chicken Alexa Fluor 555, donkey anti-rabbit Alex Fluor 647, and donkey anti-chicken Alex Fluor 488 and all secondary antibodies were used at 1:500 dilution.

Image acquisition and quantification

Slices were imaged using an Olympus BX53 fluorescent microscope with UPlanSApo 4x, 10x or 20x or a Nikon A1R confocal microscope with 20X or 60X. All images were processed and quantified with ImageJ. Cell numbers were quantified manually, since the distribution of spinal cord projection neurons is relatively sparse. Average axon density was calculated by DEFiNE, as described before.[73] Fluorescence spatial distribution of manually selected image area was quantified by plot profile in ImageJ and curves of fluorescence distribution were smoothed in Prism.

Whole mouse brain processing and imaging

Whole mouse brains were processed following the SHIELD protocol (LifeCanvas Technologies).[74] Samples were cleared for 1 day at 42°C with SmartBatch+ (LifeCanvas Technologies), a device employing stochastic electrotransport.[75] Brain samples (Figures 2A–2F) were stained with primary antibody, 10 mg of goat anti-GFP antibody (Encor, GPCA-GFP) and 10 mg of rabbit anti-RFP antibody (Rockland, 600-401-379) followed by fluorescently conjugated secondaries in 3:2 primary: secondary molar ratio (Jackson ImmunoResearch). After active labeling, samples were incubated in EasyIndex (LifeCanvas Technologies) for refractive index matching (RI = 1.52) and imaged at 3.6X with a SmartSPIM axially-swept light sheet microscope (LifeCanvas Technologies, resolution 1.8 mm × 1.8 mm x,y with a 4 mm z-step).

Fos induction

Mice were single housed at least one day before the experiment. Mice were injected with 5 mg/kg CNO intraperitoneally and placed back to their home cage. Mice were then perfused 2 h after CNO injection and tissues were processed for immunohistochemical analysis as described above.

Electrophysiology

Mice (9–11 week old) were deeply anesthetized with sodium pentobarbital (60 mg/kg) and perfused with ice-cold dissection solution consisting of (in mM): 250 sucrose, 2.5 KCl, 25 $NaHCO_3$, 1.0 NaH_2PO_4, 6 $MgCl_2$, 0.5 $CaCl_2$, and 25 glucose continuously bubbled with 95% O_2/5% CO_2. The lumbar spinal cord was isolated and immersed in low-melting-point agarose (3% in above solution; Life Technologies) and cooled on ice. Parasagittal slices (350–400 μm) with the L3-L4 dorsal roots attached (length 7–10 mm) were cut from the left side of the spinal cord using a vibrating microtome (7000smz-2; Campden Instruments). Slices were incubated for 15–20 min in a recovery solution containing (in mM): 92 NMDG, 2.5 KCl, 1.2 NaH_2PO_4, 30 $NaHCO_3$, 20 HEPES, 25 glucose, 5 Na ascorbate, 2 thiourea, 3 Na pyruvate, 10 $MgSO_4$, and 0.5 $CaCl_2$ and then allowed to recover further in an oxygenated artificial cerebrospinal fluid (aCSF) solution containing the following (in mM): 125 NaCl, 2.5 KCl, 25 $NaHCO_3$, 1.0 NaH_2PO_4, 1.0 $MgCl_2$, 2.0 $CaCl_2$, and 25 glucose for $\geq$1 h at room temperature.

After recovery, slices (with attached dorsal roots) were transferred to a submersion-type recording chamber (RC-22; Warner Instruments) and mounted on the stage of an upright microscope (BX51WI; Olympus). Slices were then perfused at room temperature with oxygenated aCSF at a rate of 2–4 mL/min and lamina I neurons projecting to the contralateral PAG, or ipsilateral parabrachial nucleus (PB), were identified via DiI or AAV1.hSyn.HI.eGFP-Cre fluorescence and visualized for patch clamp recording via infrared illumination.

Patch electrodes were constructed from thin-walled single-filamented borosilicate glass (1.5 mm outer diameter; World Precision Instruments) using a microelectrode puller (P-97; Sutter Instruments). Pipette resistances ranged from 4 to 6 MΩ and seal resistances were >1 GΩ. Patch electrodes were filled with an intracellular solution containing (in mM): 130 K-gluconate, 10 KCl, 10 HEPES, 10 Na phosphocreatine, 4 MgATP, and 0.3 Na_2GTP, pH 7.2 (295–300 mOsm). Whole-cell patch clamp recordings were obtained from projection neurons residing in lamina I of the L3/L4 dorsal horn using a Multiclamp 700B amplifier (Molecular Devices). The resting membrane potential (V_{rest}) was measured as the mean of the membrane potentials (excluding periods of action potential firing) observed during a continuous 90 s period beginning ~2 min after establishment of the whole-cell recording configuration. Membrane capacitance was measured using the built-in membrane test function in pClamp.

Excitatory postsynaptic currents (EPSCs) were evoked from a holding potential of −70 mV by electrical stimulation of the dorsal root (10–300 μA, 100 μs at a frequency of 0.067 Hz) delivered via a suction electrode connected to a constant-current stimulator (Master-8; A.M.P.I.). The threshold to evoke an EPSC was defined as the current intensity which evoked a measurable EPSC in $\geq$50% of the trials. The stimulus threshold and onset latency of an evoked EPSC were jointly used to classify the observed synaptic response as mediated by Aβ fibers, Aδ fibers, low-threshold C fibers or high-threshold C fibers, guided by information subsequently gained from compound action potentials (CAPs) recorded from the dorsal roots.[76] EPSCs mediated by Aβ fibers were classified as monosynaptic based on their ability to follow repetitive stimulation (20 Hz) with a constant latency and absence of failures, while Aδ fiber- and C fiber-mediated EPSCs were considered monosynaptic if no failures were observed during 2 Hz and 1 Hz stimulation,

respectively. Subsequently, primary afferent-evoked action potential (AP) firing was quantified as the number of APs discharged in a 1 s period following dorsal root stimulation (at a duration of 100 ms) at two intensities: (1) the threshold to evoke the observed monosynaptic EPSC; and (2) at a maximum intensity (300 μA) sufficient to activate all classes of primary afferent fibers. Firing frequency was also calculated as a peak instantaneous firing frequency (in Hz; defined as 1/minimum interspike interval), while firing duration was calculated as the time elapsed (in ms) between the first and last APs evoked by dorsal root stimulation during the 1-s sampling period. GABAergic and glycinergic transmission were not blocked in order to avoid excessive spontaneous action potential discharge in the slice.

Membrane potentials were corrected for the liquid junction potential (−14 mV) which was calculated using JPCalc software (P. Barry, University of New South Wales, Sydney, Australia; modified for Molecular Devices). Data were filtered at 4–6 kHz through a −3 dB, four-pole low-pass Bessel filter, digitally sampled at 20 kHz, and stored on a personal computer (Dell) using a commercially available data acquisition system (Digidata 1440A with pClamp 10.6 software; Molecular Devices).

Behavior

All behavior assays were performed blinded to all conditions (control or manipulation group) throughout data acquisition and analysis. For chemogenetic experiments, CNO was delivered at the dose of 5 mg/kg for hM4D experiments and 2.5 mg/kg for hM3D experiments. After behavioral experiments, brain and spinal cord tissues were collected to confirm virus injection and fiber implantation. Data from mice with poor viral expression or off-target fiber implantation were identified in a blinded manner and excluded prior to analysis.

CNO invoked spontaneous behavior

Immediately after CNO injection, mice were placed in a small chamber with video recording for at least 60 min. Unless stated otherwise, right spinal neurons were targeted for manipulation and so behavior toward the right hindpaw was quantified manually from 10 min to 30 min after CNO injection. Mice lifting their hindpaw for over 1 s or quickly shaking their hindpaw were quantified as one episode of flinching/guarding behavior. Licking behavior was defined when mice licked their hindpaw. Hindlimb-oriented behavior was quantified when mice licked their hindpaw, and forelimb-oriented behavior was quantified when mice licked their forepaw/forearm.

Open field

Mice were placed in an activity chamber (27.3 cm × 27.3 cm x 20.3 cm, Med Associates) after CNO injection and their activity was recorded for an hour with an automated recording device (Limelight software, Actimetrics). Animal location and activity were recorded by infrared beam break around the chamber and all parameters were analyzed automatically by software Fusion v.6 for Versamax (Omnitech Electronics Incorporated) with 5 min sampling intervals. Traveling distance and freezing time (immobile time) from 30 min to 60 min after CNO application were summed and analyzed.

Formalin pain test

Mice were placed in a plastic chamber on a glass board 30 min after CNO injection. Then, mice were injected with 10 μL 2% formalin. Cameras were set up below the glass board to record behavior with a bottom-up view for 60 min after formalin injection. Acute phase was defined 0–5 min after formalin injection and second phase was defined 5–60 min after formalin injection. Licking duration toward the injected hind paw was quantified.

Hargraves test

Mice were habituated on a glass plate held at 30°C (Model 390 Series 8, IITC Life Science Inc.). A radiant heat source was applied to the hind paw, and the latency to withdrawal was recorded. Three trials were conducted on each paw, with at least a 5-min interval between trials of opposite paws and a 10-min interval between trials of the same paws. A cutoff latency of 20s was set and the average withdrawal latency of both paws was calculated.

Cold plantar assay

Mice were acclimated on a glass plate and a code probe was made by packing finely crushed dry ice into a modified 3mL syringe. The cold stimuli were applied beneath the glass plate and the latency of withdrawal was recorded. Three trials were conducted on each paw, with at least a 5-min interval between trials of opposite paws and a 10-min interval between trials of the same paws. A cutoff latency of 20s was set to avoid damage and the average withdrawal latency of both paws across trials was calculated.

Tail flick

Mice were habituated to restraints 10–15 min for 5 days before testing. Tails were immersed 3 cm into a water bath at 55°C, and the latency to tail flick was measured three times per temperature with a 1-min interval between trials.

Hotplate

Mice were placed on a 52°C or 55°C hot plate and the latency to the first nociceptive response (flinching, jumping, or licking) was recorded. Licking episodes are quantified during a 60s period.

Rotarod

Mice were placed on drums that turned at the accelerating rate from 4 to 40 rpm during the trial. The time that mice were able to balance on these drums without falling was assessed. When the mice dropped onto the individual sensing platforms below, test results were recorded and mice were placed back to their home cage. Three consecutive trials were conducted and average results were recorded.

Gait analysis

Mice were placed into a walking compartment and the treadmill was turned on at the speed of 16.7 cm/s. A camera was set beneath the treadmill to record the gait. Videos of around 4 s per mouse were recorded once mice moved fluidly and maintained the treadmill speed. Recorded videos were further analyzed with DigiGait (Mouse Specifics, Inc) to quantify stride, stance and swing duration as well as stride/axial length.

Balance beam

Fine motor coordination was assessed with a raised balance beam (5 mm wide square beam). 30 min after CNO injection, mice were placed on the beam and trained to walk on the beam. After the first training trial, 3 testing trials were conducted with camera recording. 1 min rest in the dark box at the end of the beam was allowed between trials. Two days after testing, the baseline performance of balance beam was tested without CNO delivery. Foot slips were recorded with a video and then counted manually.

Optogenetic behavioral experiments

All mice with optical fiber implantation would recover for at least one week before behavioral assays. Optogenetic stimulation parameters were as follows: 10 mW, 20 Hz, 5 ms duration pulses.

Optogenetic stimulation induced spontaneous behaviors

Mice were placed in a plastic chamber for 3 min for habituation before delivering any light stimulation. All behaviors were recorded with a camera. Light stimulation lasted for 30 s. A total of three or four stimulus trains were delivered with 2 min intervals. Spontaneous behaviors including flinching/guarding and licking (described before) were quantified manually.

Optogenetic stimulation induced escaping behaviors

Mice were habituated in a customer made chamber (25.4 cm W x 36.3 cm L) for 3 min before three 30 s optogenetic stimulation bouts with 2 min intervals. Behavior was recorded with a camera and the traveling distance during stimulation was analyzed with MATLAB after body position was determined by an open source software Optimouse.[77] Post-stimulation freezing behavior was quantified as the percent of immobile time that was observed from 0 to 30 s following optogenetic stimulation.

Real time place aversion

Mice were habituated to a custom-made, two-sided chamber (25.3 cm × 36.3 cm). On the first day, mice were acclimated to the apparatus for 20 min and time spent in each chamber was recorded. On the second day, the optogenetic laser was turned on when mice entered one side of the chamber, and turned off when they entered the other. Time mice spent in the light-paired side was processed and calculated with MATLAB and Optimouse as described above.

QUANTIFICATION AND STATISTICAL ANALYSIS

GraphPad Prism, MATLAB and Microscope Excel were used for statistical analysis. Data were presented as mean ± SEM. Significance was indicated by $p \leq 0.05$. The number of animals and statistical tests were described in corresponding figure legends. Sample sizes were determined based on previous work from our lab and others.